Atmos. Chem. Phys., 25, 3011–3028, 2025
https://doi.org/10.5194/acp-25-3011-2025


Atmospheric Chemistry and Physics
Open Access
EGU

Research article

# Accurate elucidation of oxidation under heavy ozone pollution: a full suite of radical measurements in the chemically complex atmosphere

**Renzhi Hu[1], Guoxian Zhang[1,2], Haotian Cai[1], Jingyi Guo[1], Keding Lu[4], Xin Li[4], Shengrong Lou[5], Zhaofeng Tan[4], Changjin Hu[1], Pinhua Xie[1,3], and Wenqing Liu[1,3]**

[1]Key Laboratory of Environment Optics and Technology, Anhui Institute of Optics and Fine Mechanics, HFIPS, Chinese Academy of Sciences, Hefei, China
[2]School of Physics and New Energy, Xuzhou University of Technology, Xuzhou, China
[3]College of Resources and Environment, University of Chinese Academy of Science, Beijing, China
[4]State Key Joint Laboratory of Environmental Simulation and Pollution Control, College of Environmental Sciences and Engineering, Peking University, Beijing, China
[5]State Environmental Protection Key Laboratory of the Formation and Prevention of Urban Air Pollution Complex, Shanghai Academy of Environmental Sciences, Shanghai, China

**Correspondence:** Guoxian Zhang (gxzhang@aiofm.ac.cn) and Pinhua Xie (phxie@aiofm.ac.cn)

Received: 7 August 2024 – Discussion started: 30 August 2024
Revised: 13 February 2025 – Accepted: 13 February 2025 – Published: 13 March 2025

**Abstract.** The Yangze River Delta (YRD) in China encountered prolonged ozone pollution in September 2020. To accurately elucidate the limitations of oxidation processes in the chemically complex atmosphere, a full suite of radical measurements (OH, $HO_2$, $RO_2$, and $k_{OH}$) was established in the YRD region for the first time. The diurnal peaks of radicals exhibited considerable variation due to environmental factors, showing ranges of 3.6 to $27.1 \times 10^6$ cm$^{-3}$ for OH, 2.1 to $33.2 \times 10^8$ cm$^{-3}$ for $HO_2$, and 4.9 to $30.5 \times 10^8$ cm$^{-3}$ for $RO_2$. The simulated results provided by RACM2-LIM1 failed to adequately match the observed data in both radical concentration and experimental budget for a heavy ozone pollution episode. Sensitivity tests utilizing a comprehensive set of radical measurements revealed that the Higher Aldehyde Mechanism (HAM) effectively complements the regeneration of OH radicals, yielding enhancements of 4.4 %–6.0 % compared to the base scenario, while the concentrations of $HO_2$ and $RO_2$ radicals have shown increments of about 7.4 % and 12.5 %, respectively. It is noteworthy that under the constraints of $k_{OH}$ measurement, the inclusion of oxygenated volatile organic compounds (OVOCs) and larger alkoxy radicals derived from monoterpenes improved the model–measurement consistency for ozone formation, reducing the discrepancy under high NO conditions from 4.17 to 2.39. This outcome corroborates the hypothesis of sensitivity analysis as it pertains to ozone formation. Moving forward, by implementing a comprehensive radical detection approach, further investigations should concentrate on a broader range of OVOCs to rectify the imbalance associated with $RO_2$ radicals, thereby providing a more precise understanding of oxidation processes during severe ozone pollution episodes.

Published by Copernicus Publications on behalf of the European Geosciences Union.

## 1 Introduction

In recent years, China's rapid economic development has led to severe environmental pollution problems, which has significantly impacted the respiratory, dermatological, and ocular health of local residents (Wang et al., 2022c; Huang et al., 2018). This has raised concerns about the coexistence of regional primary and secondary pollution, making air quality improvement efforts a focal point (Liu et al., 2021; Wang et al., 2022a). In the complex atmosphere, near-surface ozone ($O_3$) is formed through continuous photochemical reactions between nitrogen oxides ($NO_x \equiv NO + NO_2$) and volatile organic compounds (VOCs) under light conditions, while hydroxyl radicals (OH) serve as the main oxidant in the troposphere, converting VOCs into hydroperoxy ($HO_2$) and organic peroxy ($RO_2$) radicals (Rohrer et al., 2014; Hofzumahaus et al., 2009). Additionally, the oxidation of nitric oxide (NO) and peroxy radicals produces nitrogen dioxide ($NO_2$), which is the sole photochemical source of ozone (Lu et al., 2012; Stone et al., 2012).

Despite numerous experimental and theoretical explorations to establish the radical-cored photooxidation mechanism in the troposphere, field observations were primarily focused on $HO_x$ ($HO_x \equiv OH + HO_2$) radicals due to the limitations of detection technology (Kanaya et al., 2012; Lu et al., 2012; Hofzumahaus et al., 2009; Kanaya et al., 2007a; Ren et al., 2008; Stone et al., 2012; Levy, 1971). Recent advancements in detection technology, such as the application of a new LIF technique (ROxLIF), have made the detection of $RO_2$ radicals possible (Whalley et al., 2013; Tan et al., 2017a). Moreover, the union of comprehensive field campaigns and box models has proven to be an effective method for verifying the integrity of radical chemistry at local to global scales (Lu et al., 2019; Tan et al., 2018). Several experiments have indicated that the existing atmospheric chemical mechanism posed challenges in deepening the understanding of the regional pollution explosion (Whalley et al., 2021; Slater et al., 2020; Tan et al., 2017a; Woodward-Massey et al., 2023). For instance, the observation of up to $4 \times 10^9$ cm$^{-3}$ of the $RO_2$ radical in the center of Beijing in 2017 (APHH) was significantly underestimated by MCM v3.3.1 (Whalley et al., 2021). Further exploring the unreproducible concentration and the oxidation process in the chemically complex atmosphere is deemed necessary (Whalley et al., 2021; Woodward-Massey et al., 2023).

The Yangze River Delta (YRD) region, situated between the North China Plain (NCP) and Pearl River Delta (PRD), is highly prone to regional transport interactions and aerosol–boundary layer feedback (Jia et al., 2021; Huang et al., 2020). In an effort to gain a better understanding between the complex radical chemistry and the intensive oxidation level in the Yangze River Delta, TROPSTECT-YRD (The experiment on Radical chemistry and Ozone Pollution perSpectively: long-Term Elucidation of the photochemiCal oxidaTion in the Yangze River Delta) was conducted in Hefei during September 2020. Accurate elucidation of the oxidation process under heavy ozone pollution was provided by a full suite of radical measurements (OH, $HO_2$, $RO_2$, and $k_{OH}$) in the chemically complex atmosphere.

## 2 Materials and methods

### 2.1 Site description and instrumentation

The TROPSTECT observation was conducted from 1 to 20 September 2020 at the Science Island background station (31.9° N, 117.2° E) in Hefei, a typical megacity located in the central region of Anhui Province within the Yangtze River Delta. The station is situated on a peninsula with abundant vegetation to the northwest of urban areas and is in close proximity to Dongpu Lake, which is only 200 m away, and the main road, positioned 250 m southward (Fig. 1). Consequently, the relatively enclosed environment exhibits typical suburban characteristics of anthropogenic emissions. The station is located in the transition region between urban and suburban areas, reflecting the regional transport of pollution in Hefei and its surrounding areas.

Regarding the instrumentation, a group of oxidation-related instruments were installed on the seventh floor of the Comprehensive Building at the Anhui Institute of Optics and Fine Mechanics (AIOFM), with all sampling outlets positioned more than 20 m above the ground. The details of the instruments measuring various parameters such as meteorological factors (WS, WD, $T$, RH, $P$, $J$ values), gas pollutants ($O_3$, CO, $SO_2$, NO, $NO_2$, HONO, HCHO, PAN), and non-methane hydrocarbons (NMHCs) are provided in Table S1 in the Supplement.

The measurement of NO, $NO_2$, $O_3$, CO, and $SO_2$ was carried out using commercial Thermo Electron model series instruments. Thereof, NO and $NO_2$ were measured using a chemical luminescence method (CL) with an enhanced trace-level NO–$NO_2$–$NO_x$ analyzer (PKU-PL), which achieved a detection limit of 50 ppt (Tan et al., 2017a). The detection of $O_3$ and $SO_2$ was conducted through Thermo Electron model 49i and 43i, respectively, while Thermo Electron model 48i was utilized for CO detection. Cavity ring-down spectroscopy (CRDS, Picarro-G2401) was employed for CO detection in parallel, and another ultraviolet absorption instrument (Ecotech EC9810B) was for ozone detection. The instrument inlets were placed within 5 m of each other for comparison.

All Thermo series gas analyzers were equipped with individual sampling inlet tubing, which was made of polyfluoroalkyl (PFA; with 6.35 mm outer diameter), and the flow rate was operated at 1.5 L min$^{-1}$. The total length of the inlet tubing from the sampling tip to the instrument inlet was 2.5 m, with the entire line wrapped with insulation material to prevent condensation of water vapor. To ensure measurement accuracy, the instruments in the campaign underwent zero-point calibration procedures during the early (31 Au-

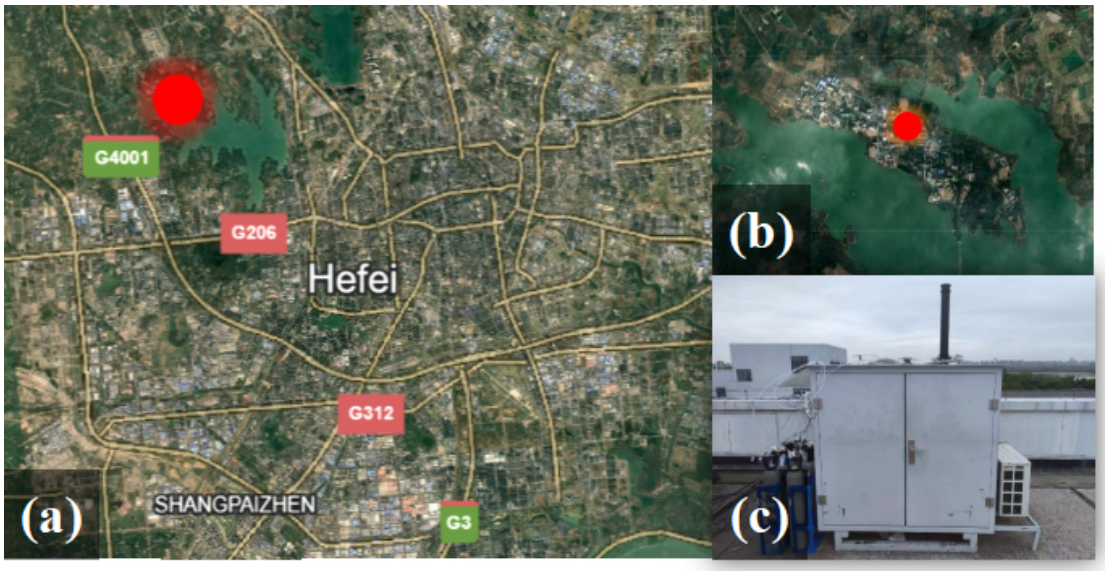


**Figure 1.** **(a)** The location of the measurement site (source: © Google Earth). **(b)** A close shot of the measurement site location (source: © Google Earth). **(c)** The actual image for the LIF box.

gust) and late (21 September) observation periods. Furthermore, additional zero calibration for Thermo 48i CO detection was undertaken daily from 00:00–00:30 UTC+8 (this time zone applies to all times mentioned in the paper) to minimize shift correction. Zero-point calibration includes the instrument and the complete inlet system. Cross-calibrations for $O_3$ and CO measurements were carried out during the middle (9 September). The comparison results revealed high consistency within the instrument accuracy range for both CO and $O_3$ measurements (Fig. S1a, b in the Supplement).

HONO was detected using a home-built instrument by cavity-enhanced absorption spectroscopy (CEAS), while formaldehyde was determined by the Hantzsch method (SDL model 4050) (Duan et al., 2018; Yang et al., 2021a). An automated gas chromatograph equipped with a mass spectrometer and flame ionization detector (GC-FID/MS) was employed for the online measurement of 99 VOC species. Information for parts of the VOC monitoring species by online GC-MS/FID is listed in Table S2.

The eight crucial photolysis frequencies ($j(NO_2)$, $j(H_2O_2)$, $j$(HCHO_M), $j$(HCHO_R), $j$(HONO), $j(NO_3\_M)$, $j(NO_3\_R)$, $j(O^1D)$) were directly measured by a photolysis spectrometer (Metcon, Germany). The unmeasured photolysis frequencies of the remaining active species were computed using Eq. (1):

$$j = l \cdot \cos(\chi)^m \cdot e^{-n \cdot \sec(\chi)}. \quad (1)$$

The variations in photolysis frequency due to solar zenith angle ($\chi$) were adjusted based on the ratio of observed and simulated $j(NO_2)$. The optimal values for parameters ($l$, $m$, and $n$) for different photolysis frequencies were extensively detailed by MCM v3.3.1 (https://mcm.york.ac.uk/MCM/rates/photolysis, last access: 12 March 2025) (Jenkin et al., 2003, 1997).

## 2.2 Radical measurement

### 2.2.1 OH, $HO_2$, $RO_2$ concentrations

The laser-induced fluorescence instrument developed by the Anhui Institute of Optics and Fine Mechanics (AIOFM-LIF) was used to simultaneously detect the concentrations of OH, $HO_2$, and $RO_2$ radicals, along with OH reactivity ($k_{OH}$). The OH radical was directly measured by detecting on-resonance fluorescence excited by a 308 nm laser. An indirect measurement for $HO_2$ was carried out after converting it to OH at a fixed efficiency (Heard and Pilling, 2003).

The laser utilized for fluorescence excitation is a high-frequency tunable dye laser that emits a 308 nm laser, with the laser power divided into a ratio of 0.45 : 0.45 : 0.08 : 0.02. Of this power, 90 % is directed towards fluorescence cells for concentration and reactivity detection via optical fibers, respectively, and 8 % of the laser power is directed to a reference cell, while the remaining 2 % is used to monitor real-time power fluctuations. The laser is transmitted through $HO_2$, OH, and $RO_2$ cells in turn via a coaxial optical path. Two photodiodes are set up at the end of the reference cell and $RO_2$ detection cell, respectively. The voltage signals and power fluctuations are compared synchronously to diagnose the laser stability. To maintain detection efficiency, the power inside the measurement cells should not be less than 10 mW. Sampling nozzles of 0.4 mm are deployed above OH and $HO_2$ cells for efficient sampling at a flow rate of approxi-

mately 1.1 slpm, and the pressure for all fluorescence cells is maintained at 400 Pa. The micro-channel plate (MCP) detects the weak fluorescence signal collected by lens systems with low noise and high gain. Additionally, a digital delay generator (DG645) optimizes the timing control between the laser output, signal detection, and data acquisition. All of these modules are integrated into a sampling box with constant air conditioning, except for the laser.

The detection of $RO_2$ radicals is more complex compared to the integrated detection of OH and $HO_2$ radicals (Whalley et al., 2013). To achieve the complete chemical conversion from $RO_x$ to $HO_2$, a crucial role is played by a 66 mm × 830 mm aluminum flow tube, whose performance has been confirmed through the CHOOSE-2019 field campaign (Li et al., 2020). A mixture of 0.17 % CO and 0.7 ppm NO injected into the flow tube facilitates the reduction of heterogeneous radical loss and enhancement of conversion efficiency. The sampling flow is limited to 7 slpm by a 1 mm nozzle, and the tube pressure is maintained at 25 hPa. In contrast to the $HO_x$ cells, the large-diameter nozzle (4 mm) is equipped above the cell, and a high concentration of NO ($\sim$ 300 ppm) facilitates the full-magnitude $HO_2 \rightarrow$ OH conversion.

The observation data ($H_2O$, $O_3$) are combined with experimental characterization to eliminate ozone photolysis interference, and most interference signals are excluded by utilizing wavelength modulation (Zhang et al., 2022a). A comparison experiment with PKU-LIF demonstrated the consistency of OH measurement in the complex atmosphere (Zhang et al., 2022b). An additional atmospheric oxidation observation was conducted in the same location and season in 2022 with a chemical modulation method to determine the chemical background of OH radicals (Fig. S2). During the ozone pollution (29 September 2022–2 October 2022), the daytime ozone concentration peaks above 75 ppb, accompanied by alkene species approaching $\sim$ 10 ppb. The diurnal concentration of isoprene was also at a high level (> 1 ppb). The chemical conditions are more favorable to induce OH interference than in the TROPSTECT campaign, while the OH concentrations achieved by chemical modulation ($OH_{chem}$) and wavelength modulation ($OH_{wav}$) were in good agreement. No obvious chemical background was observed by deploying an inlet pre-injector. While it was not anticipated that OH measurements would be influenced by internal interference, the possibility of unknown interferences cannot be excluded since titration tests were not employed during the campaign. Consequently, the OH measurements represent an upper bound to the actual values.

For $HO_2$ measurement, lower NO concentrations ($\sim 1.6 \times 10^{12}$ cm$^{-3}$, corresponding to $\sim$ 15 % conversion efficiency) are selected to limit the $RO_2 \rightarrow HO_2$ interference to less than 5 % (Wang et al., 2021). Since only the total-$RO_2$ mode is used for the campaign, the additional uncertainty introduced by $RO_2$ / $R(OH)O_2$ classification is negligible (Tan et al., 2017b). The observed maximum daily PAN (11:00–14:00) is only $1.15 \pm 0.67$ ppb, resulting in a calculated PAN-pyrolytic interference for $RO_2$ measurement of less than 1 ppt (Fuchs et al., 2008). The general applicability of AIOFM-LIF in the complex atmosphere has been demonstrated through various campaigns (Zhang et al., 2022b; Wang et al., 2021; Wang et al., 2019a).

To complete the calibration task, a standard source stably generates equal amounts of OH and $HO_2$ radicals (Wang et al., 2020). The radical source is also capable of yielding specific $RO_2$ by titrating hydrocarbon with OH. It is noteworthy that $CH_3O_2$ has the highest mixing ratio in the $RO_2$ species, thus it was chosen to represent sensitivity calibration. The instrument is calibrated every 2 d, except during rainy weather. The limit of detection (LOD) for OH, $HO_2$, and $RO_2$ in different cells with a typical laser power of 10 mW is measured at $3.3 \times 10^5$, $1.1 \times 10^6$, and $2.5 \times 10^6$ cm$^{-3}$, respectively (60 s, 1$\sigma$). Measurement accuracy for OH, $HO_2$, and $RO_2$ radicals is reported to be 13 %, 17 %, and 21 %, respectively.

### 2.2.2 OH reactivity ($k_{OH}$)

The detection of $k_{OH}$ in the atmosphere, defined as the reciprocal of OH lifetime, was conducted using a laser flash photolysis laser-induced fluorescence (LP-LIF) instrument (Lou et al., 2010). The configuration structure for $k_{OH}$ measurement has been detailed in a previous study (Liu et al., 2019). The flow tube in the OH production–reaction unit is at ambient pressure, with a gas flow rate of 17 slpm. A pulsed laser beam (266 nm with an average power of 15 mJ) is output from a frequency-quadrupled Nd:YAG laser, which generates stable OH radical through flash photolysis of ambient ozone in the flow tube. Consistent and stable production of OH radicals is ensured by maintaining a stable concentration of reactants, flow field, and laser energy. Under conditions of 80 ppb $O_3$ and 8000 ppm water vapor concentration, OH radicals produced in the flow tube remain at the concentration order of $10^9$ cm$^{-3}$. Subsequently, the OH radicals are sampled through a nozzle into a fluorescence cell. The OH fluorescence signal is then detected using laser pump and probe techniques and is fitted to calculate the slope of OH decay ($k_{OH}$). The detection accuracy, achieved with an integration time of 180 s, is 0.3 s$^{-1}$ (1$\sigma$).

## 2.3 Observation-based model

The Regional Atmospheric Chemical Mechanism version 2 (RACM2) incorporating the latest Leuven isoprene mechanism (LIM) was utilized to simulate the concentrations and reactions of OH, $HO_2$, and $RO_2$ radicals (Stockwell et al., 1997; Griffith et al., 2013; Peeters et al., 2014). RACM2-LIM1 was specifically involved with fewer species compared to the explicit MCM, thus ensuring higher operational efficiency (Liu et al., 2022). The comprehensive list of model constraints is provided in Table S3. The measured NMHCs

include 29 alkanes, 11 alkenes, and 15 aromatics, as well as acetylene and isoprene. For the base scenario, boundary conditions were established using the observed species, with assumed concentrations of hydrogen ($H_2$) and methane ($CH_4$) at 550 and 1900 ppb, respectively. An ozone-simulation test was conducted to determine the suitable depositional lifetime ($\tau_D$) for the species involved in the base model. At the lifetime of 24 h, with a corresponding first-order loss rate of 1.1 cm $s^{-1}$ (assuming a boundary layer height of 1 km), the simulated ozone concentration closely matched the observed values (Fig. S3). The time resolution of all constraints was uniformly set to 15 min through averaging or linear interpolation. To reinitialize unconstrained species to a steady-state, 3 d of data was input in advance as the spin-up time.

To improve the model–measurement consistency between OH, $HO_2$, and $RO_2$ radicals, a series of sensitivity analyses were performed to evaluate the impacts of potential mechanisms, as detailed in Table 1. The Higher Aldehyde Mechanism (HAM) was introduced to discuss the influence of reactive aldehyde chemistry, and additional monoterpene species (MTS) was employed to represent the complex isomerization steps experienced by $RO_2$ radicals derived from other unmeasured VOCs. Reactions involving monoterpene and HAM are listed in Tables S4 and S5. Furthermore, under the framework of the base model, another investigation on the photochemical role of unmeasured oxygenated volatile organic compound (OVOC) species in the atmosphere was conducted by MCM v3.3.1.

The local formation of ozone can be accurately quantified through the online measurement of $RO_x$ radicals (Tan et al., 2018). To overcome the interference from NO, the total oxidant ($O_x$), which is defined as the sum of $NO_2$ and $O_3$, can serve as a reliable parameter to indicate the level of oxidation. Equation (2) shows that the rate of NO oxidation by peroxy radicals is equivalent to the production of $O_3$, denoted as $F(O_x)$:

$$F(O_x) = k_{HO_2+NO}[NO][HO_2] + \sum\nolimits_i k_{RO_2^i+NO}[NO]RO_2^i. \quad (2)$$

The major loss pathways for $O_x$ encompass ozone photolysis, ozonolysis reactions, and radical-related reactions ($OH / HO_2 + O_3$, $OH + NO_2$) are represented as $D(O_x)$ in Eq. (3):

$$\begin{aligned} D(O_x) = {} & \varphi_{OH} j(O^1D)[O_3] \\ & + \Sigma i \{\varphi^i_{OH} k^i_{Alkenes+O_3}[Alkenes][O_3]\} \\ & + (k_{O_3+OH}[OH] + k_{O_3+HO_2}[HO_2])[O_3] \\ & + k_{OH+NO_2}[OH][NO_2]. \end{aligned} \quad (3)$$

Here, the OH yields from ozone photolysis and ozonolysis reactions are denoted as $\varphi_{OH}$ and $\varphi^i_{OH}$, respectively.

The net photochemical $O_x$ production rate in the troposphere, denoted as $P(O_x)$ in Eq. (4), can therefore be calculated as the difference between Eqs. (2) and (3):

$$P(O_x) = F(O_x) - D(O_x). \quad (4)$$

## 2.4 Experimental budget analysis

In this study, an experimental radical budget analysis was also conducted (Eqs. 5–12). Unlike model studies, this method relies solely on field measurements (concentrations and photolysis rates) and chemical kinetic data, without depending on concentrations calculated by models (Whalley et al., 2021; Tan et al., 2019b). Given the short-lived characteristics of OH, $HO_2$, and $RO_2$ radicals, it is expected that the concentrations are in a steady state, with total production and loss rates being balanced (Lu et al., 2019). By comparing the known sources and sinks for radicals, unknown processes for initiation, transformation, and termination can be determined.

$$\begin{aligned} P(OH) = {} & j_{HONO}[HONO] + \varphi_{OH} j(O^1D)[O_3] \\ & + \Sigma i \{\varphi^i_{OH} k^i_{Alkenes+O_3}[Alkenes][O_3]\} \\ & + (k_{HO_2+NO}[NO] + k_{HO_2+O_3}[O_3])[HO_2] \end{aligned} \quad (5)$$

$$D(OH) = [OH] \times k_{OH} \quad (6)$$

$$\begin{aligned} P(HO_2) = {} & 2 \times j_{HCHO\_R}[HCHO] \\ & + \Sigma i \{\varphi^i_{HO_2} k^i_{Alkenes+O_3}[Alkenes][O_3]\} \\ & + (k_{HCHO+OH}[HCHO] + k_{CO+OH}[CO])[OH] \\ & + \alpha k_{RO_2+NO}[NO][RO_2] \end{aligned} \quad (7)$$

$$\begin{aligned} D(HO_2) = {} & (k_{HO_2+NO}[NO] \\ & + k_{HO_2+O_3}[O_3] + k_{HO_2+RO_2}[RO_2] \\ & + 2 \times k_{HO_2+HO_2}[HO_2])[HO_2] \end{aligned} \quad (8)$$

$$\begin{aligned} P(RO_2) = {} & \Sigma i \{\varphi^i_{RO_2} k^i_{Alkenes+O_3}[Alkenes][O_3]\} \\ & + k_{OH}[VOCs][OH] \end{aligned} \quad (9)$$

$$\begin{aligned} D(RO_2) = {} & \{(\alpha + \beta) k_{RO_2+NO}[NO] \\ & + (2 \times k_{RO_2+RO_2}[RO_2] \\ & + k_{HO_2+RO_2}[HO_2])\}[RO_2] \end{aligned} \quad (10)$$

$$\begin{aligned} P(RO_x) = {} & \Sigma i \{(\varphi^i_{OH} + \varphi^i_{HO_2} + \varphi^i_{RO_2}) k^i_{Alkenes+O_3} \\ & [Alkenes][O_3]\} + j_{HONO}[HONO] \\ & + \varphi_{OH} j(O^1D)[O_3] + 2 \times j_{HCHO\_R}[HCHO] \end{aligned} \quad (11)$$

$$\begin{aligned} D(RO_x) = {} & (k_{OH+NO_2}[NO_2] + k_{OH+NO}[NO])[OH] \\ & + \beta k_{RO_2+NO}[NO] \\ & + 2 \times (k_{RO_2+RO_2}[RO_2][RO_2] \\ & + k_{HO_2+RO_2}[HO_2][RO_2] \\ & + k_{HO_2+HO_2}[HO_2][HO_2]), \end{aligned} \quad (12)$$

where $j(HONO)$ and $j(O^1D)$ are the measured photolysis rates of HONO and $O_3$, respectively, and $j(HCHO\_R)$ is the measured photolysis rate for the channel of formaldehyde photolysis generating $HO_2$. $\varphi_{OH}$ represents the OH yield in the $O_3$ photolysis reaction. $\varphi^i_{OH}$, $\varphi^i_{HO_2}$, and $\varphi^i_{RO_2}$ are the yields for the ozonolysis reaction producing OH, $HO_2$, and $RO_2$, respectively. $\alpha$ is the proportion of $RO_2$ radicals reacting with NO that are converted to $HO_2$, and $\beta$ is the propor-

**Table 1.** The sensitive test scenarios utilized to improve the model–measurement consistency between OH, $HO_2$, and $RO_2$ radicals.

| Scenario | Configuration | Purpose |
|---|---|---|
| Base | RACM2 updated with isoprene reaction scheme (LIM) | The base case with the species involved in Table S3 are constrained as boundary conditions. |
| MCM on | As the base scenario, but the reaction scheme is replaced by MCM v3.3.1. | To assess the photochemical role of unmeasured OVOC species in the atmosphere. |
| HAM on (4 × ALD) | As the base scenario but with the reactive aldehyde chemistry added, and the concentration of ALD is amplified by a factor of 4. | To quantify the impact of missing aldehyde primary emissions on $RO_x$ chemistry. |
| HAM on (4 × ALD + MTS) | As the HAM on (4 × ALD) scenario, but a monoterpene source is added, and the monoterpene level is ∼ 0.4 ppb. | Utilizing monoterpene-derived $RO_2$ to represent the alkoxy radicals with rather complex chemical structures. |
| Ozone simulation | As the base scenario, but the constraints of the observed ozone and NO concentrations are removed. | To test the suitable lifetime for the base model. |
| HCHO simulation | As the base scenario, but the constraints of the observed HCHO concentration are removed. | To test the simulation effect of the existing mechanism on formaldehyde concentration. |

tion of alkyl nitrate formation, which are set to 1 and 0.05, respectively (Tan et al., 2019b).

## 3 Results

### 3.1 Overview of measurement

The meteorological parameters and trace gas concentrations during the observation period are plotted in Fig. S4. The time series revealed that the peak temperature exceeded 30 °C, and the humidity levels remained between 30 %–50 % during the daytime. The photolysis rates were observed to peak at noon (11:00–13:00), with $j(O^1D)$ and $j(NO_2)$ reaching approximately $3 \times 10^{-5}\ s^{-1}$ and $8 \times 10^{-3}\ s^{-1}$, respectively. Brief rainfall events temporarily happened on 10, 15, and 17 September, but very favorable meteorology induced the prolonged ozone pollution. The daily maximum 8 h average ozone concentration (MDA8), as depicted in Fig. 2, consistently exceeded the Chinese Grade I national air quality standard (GB3095-2012) throughout the observation, with 9 d exceeding the Grade II standard.

The ozone pollution can be categorized into three continuous periods based on pollution levels, which display transitional "Semi–Heavy–Semi" pollution characteristics. Figure 3 depicts daily variations in meteorological and trace gas concentrations for different periods. During Semi I (1 to 5 September) and Semi II (11 to 14 September) periods, the MDA8 levels exceeded the Grade I standard, with an average value of $75.92 \pm 5.14$ and $75.45 \pm 3.73$ ppb, respectively. Notably, NO levels peaked around 09:00 and rapidly decreased to a few hundred parts per trillion (ppt) due to photochemistry. In addition, HONO and $NO_2$ exhibited bimodal variations, with diurnal concentration ranges of 0.09–0.50 and 3.35–13.77 ppb, respectively. The HONO / $NO_2$ ratios during both Semi periods were consistent with previous urban/suburban observations, with daytime values of $0.049 \pm 0.014$ and $0.035 \pm 0.012$, respectively (Yang et al., 2021b; Shi et al., 2020; Hu et al., 2022). Isoprene levels accumulated during the day and decreased at night during both Semi pollution episodes, with a diurnal average concentration in Semi II only 49.3 % of that in Semi I ($0.71 \pm 0.087$ ppb vs $0.35 \pm 0.073$ ppb). Formaldehyde, as the key oxidation species, exhibited a concentration profile mirroring that of isoprene, with significantly higher concentrations ranging from 1.20 to 36.34 ppb compared to other urban regions (Ma et al., 2022; Yang et al., 2022; Tan et al., 2017b; Yang et al., 2021a). Heavy pollution episodes from 5 to 9 September resulted in daytime ozone concentration as high as 129.9 ppb, and oxidation-related species such as HCHO, HONO, $NO_x$, and VOCs increased synchronously compared to other days.

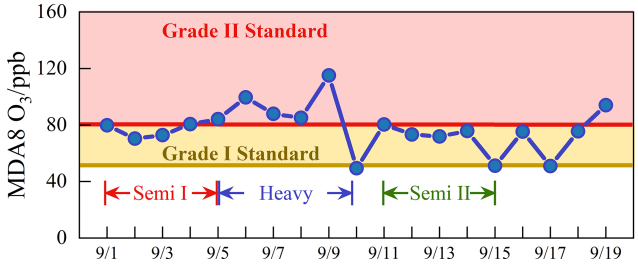


**Figure 2.** The daily maximum 8 h average $O_3$ during the campaign. The yellow and red lines denote the Grade I and Grade II national standards for $O_3$, respectively. Brief rainfall events temporarily happened on 10, 15, and 17 September.

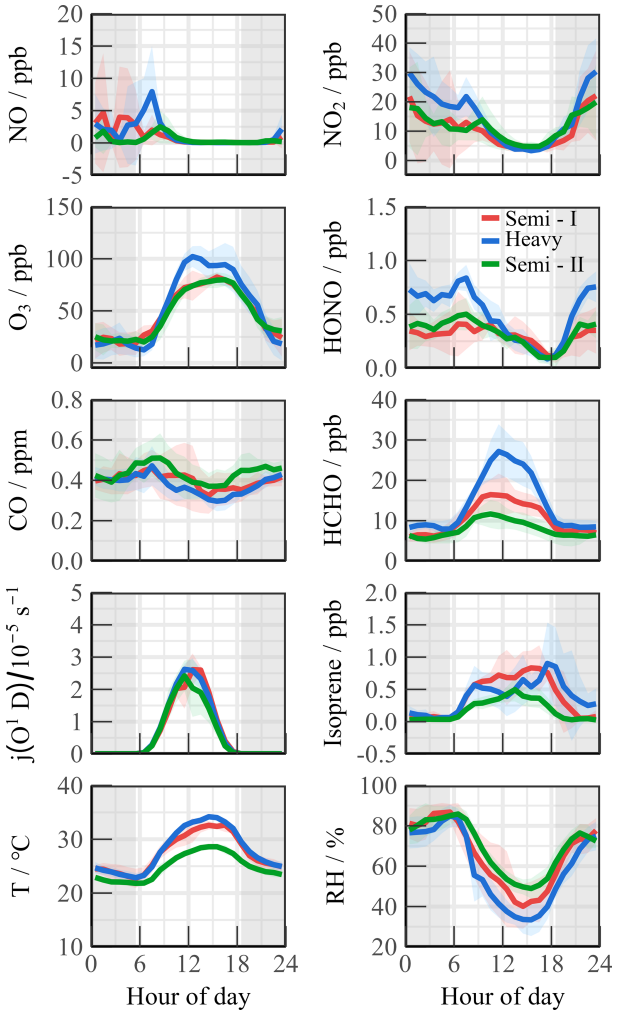


**Figure 3.** Mean diurnal profiles of observed meteorological and chemical parameters during the campaign. Three periods were divided for subsequent study (Semi I, Heavy, and Semi II).

### 3.2 $RO_x$ radical concentrations and budgets

The observed and modeled time series for OH, $HO_2$, $RO_2$, and $k_{OH}$ during the observation time are depicted in Fig. 4. The diurnal peaks of radicals exhibited a wide span due to changes in environmental conditions, with ranges of 3.6–$27.1 \times 10^6$ cm$^{-3}$ for OH, 2.1–$33.2 \times 10^8$ cm$^{-3}$ for $HO_2$, and 4.9–$30.5 \times 10^8$ cm$^{-3}$ for $RO_2$. Continuous data for $k_{OH}$ observation were acquired within a range of 8.6–30.2 s$^{-1}$. Figure S5 presents the diurnal profiles of the observed and modeled values during different episodes. The diurnal maximum of OH radical at noon differed between Semi I and Semi II, with $9.28 \times 10^6$ and $5.08 \times 10^6$ cm$^{-3}$, respectively, while total peroxy radicals ($HO_2 + RO_2$) remained at similar levels with $19.43 \times 10^8$ and $18.38 \times 10^8$ cm$^{-3}$. Additionally, the distribution of peroxy radicals is not similar in the two Semi periods, with $HO_2$ / $RO_2$ ratios of 1.69 : 1 and 0.76 : 1, respectively, which reflects the uneven oxidation levels between Semi I and Semi II. During the Heavy ozone pollution, the averaged OH, $HO_2$, and $RO_2$ concentrations were 1.90, 2.15, and 1.98 times higher than those in the Semi periods, suggesting a stronger oxidation capacity, with $k_{OH}$ in Heavy being 26.43 % and 9.56 % higher than in Semi I and Semi II, respectively. Limited anthropogenic emissions in the suburban environment reduced the oxidation contribution by $NO_x$ and CO (27.59 %). During the heavy pollution, organic species exhibited dominant behavior regarding diurnal reactivity (9.22 s$^{-1}$ for 69.79 %), and anthropogenic hydrocarbons were not major $k_{OH}$ sources. With an abundant level (∼ 1 ppb), isoprene contributed more than 10 % of the reactivity in the diurnal cycle. Therefore, the effect of biogenic VOC (BVOC) species (such as monoterpenes and limonene) on radical chemistry cannot be ignored (Ma et al., 2022; Wang et al., 2022b). $k_{OVOCs}$ are categorized into three groups: $k_{OVOCs(Obs)}$, $k_{OVOCs(Model)}$, and $k_{HCHO}$. Given the significance of formaldehyde photolysis, the contribution of HCHO to $k_{OVOCs}$ is established. $k_{OVOCs(Obs)}$ encompasses species observed in addition to formaldehyde, such as acetaldehyde (ACD) and the oxidation products of isoprene (MACR and MVK). Intermediates generated by the model, including glyoxal (GLY), methylglyoxal (MGLY), higher aldehydes (ALD), ketones (KET), methyl ethyl ketone (MEK), and methanol (MOH), are classified as $k_{OVOCs(Model)}$. Upon considering $k_{OVOCs(Model)}$ calculated by RACM2-LIM1, the reactivity calculated prior to 10 September aligns quite well with the observed OH reactivity.

The significant variations in oxidation can be inferred from the disparities during different pollution periods (Fig. S5). During Semi I, there was good agreement between the measurement and model data for peroxy radicals during the daytime. RACM2-LIM1 effectively replicated the morning OH radical concentration. However, following 10:00, NO gradually declined, and the increasing OH concentration could not be accounted for by the $HO_2 + NO$ formation channel, resulting in a maximum underestimation of $5.85 \times 10^6$ cm$^{-3}$ (Hofzumahaus et al., 2009; Lu et al., 2012). In the Semi II episode, OH was not underestimated in the low NO regime, with a slight overestimation of $HO_2$ concentration. However, the simulated $RO_2$ concentration was only $3.78 \times 10^8$ cm$^{-3}$, whereas observations were 2.77 times larger than the simulation, indicating the existence of additional reaction pathways that likely propagated the OH → $RO_2$ conversion efficiency. A significant discrepancy of radicals existed in the heavy ozone concentration, with OH, $HO_2$, and $RO_2$ radicals concurrently underestimated at noon by $8.23 \times 10^6$, $3.94 \times 10^8$, and $11.59 \times 10^8$ cm$^{-3}$, respectively. The observed $HO_2$ / $RO_2$ ratio approached 1 : 1, while the model reflected an unreasonable ratio of 3 : 1, indicating deficiencies in both primary sources and secondary propagation. The calculated reactivity seems to compare well with the observed OH reactivity at the start of the measurement period, but then there is evidence of missing OH reactivity after 10 Septem-

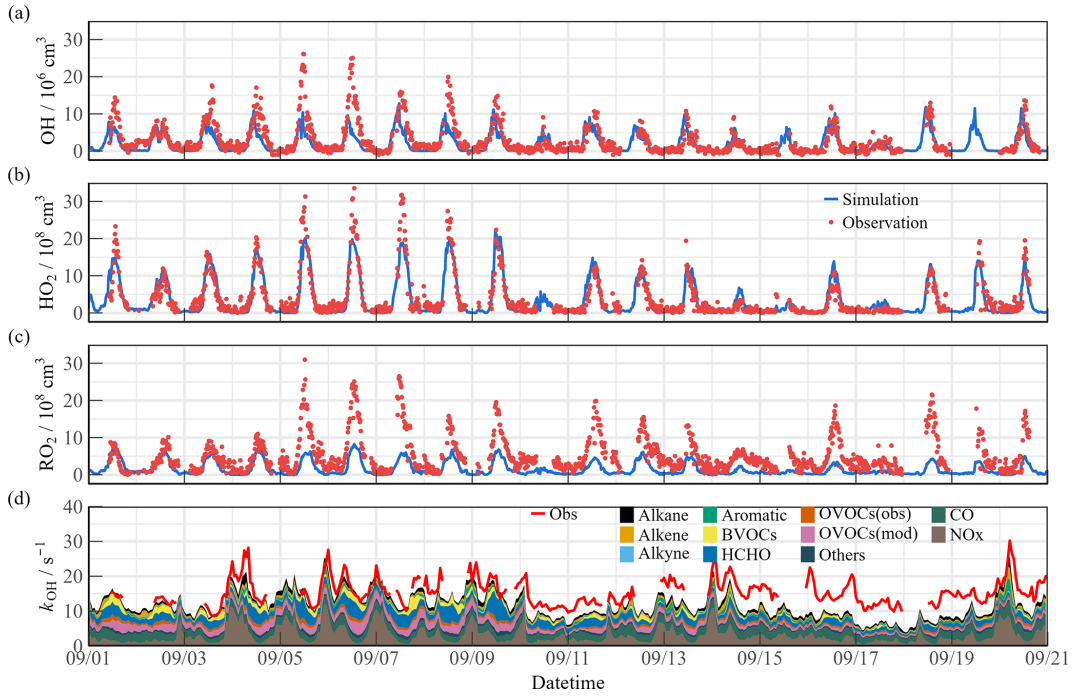


**Figure 4.** Time series of the observed and modeled parameters for **(a)** OH, **(b)** $HO_2$, **(c)** $RO_2$, and **(d)** $k_{OH}$ during the observation period.

ber (Fig. 4d). Due to the limitations of available instruments, this observation only measured a limited number of OVOC species, making it difficult to accurately quantify the contribution of larger aldehydes and ketones, carboxylic acids, nitrophenols, and other multifunctional species to $k_{OH}$ (Wang et al., 2024). Since the MCM considers more secondary formation reactions than RACM2, it can qualitatively assess the photochemical role of unmeasured OVOC species in the atmosphere (Wang et al., 2022d). The additional modeled OVOCs by MCM v3.3.1 contributed $\sim 2.4\ s^{-1}$ to the missing OH reactivity (Fig. S6). During the Heavy period, the reactivity of more model oxidation products increased the daytime $k_{OH}$ by about $5.1\ s^{-1}$. Therefore, the observed $k_{OH}$ can serve as an upper limit for sensitivity tests, and the full suite of radical measurements can be performed to explore the missing oxidation properties and ozone formation (Sect. 4.1).

Figure 5 displays the diurnal profiles of the $RO_x$ budget during different episodes. In Semi I, formaldehyde photolysis showed a higher contribution (38.6 %), while HONO photolysis (21.0 %) and ozone photolysis (24.7 %) accounted for similar proportions in primary sources. The contribution of photolysis from other OVOCs was comparable to that of ozonolysis reactions (7.2 % vs. 4.8 %). However, in Semi II, the decreased oxidation level was attributed to lower $RO_x$ sources, despite the similar proportions. During the Heavy period, the primary sources dramatically increased (up to $\sim 10\ ppb\ h^{-1}$), with HCHO photolysis contributing the most, alongside other sources at common levels (ranging between 1.74–2.66 $ppb\ h^{-1}$) in the YRD region (Ma et al., 2022). Fast HCHO oxidation dominated the radical primary source during heavy ozone pollution, which contrasts with the dominant role of $HONO / O_3$ in other megacities (Yang et al., 2022; Tan et al., 2017b; Yang et al., 2021a).

The radical removal rate during the daytime was generally balanced with production contributions. In the morning, owing to high $NO_x$ concentrations, radical termination was mainly dominated by $OH + NO_2$, $OH + NO$, $RO_2 + NO$, and $RO_2 + NO_2$. Furthermore, the formation of peroxy nitrate accounted for a certain proportion ($\sim 5$ %). As $NO_x$ concentrations decreased after 10:00, self-reactions in peroxy radicals became significant.

By comparing the known sources and sinks for radicals, unknown processes for initiation, transformation, and termination can be determined in the experimental budget analysis (Fig. S7). During the Semi I period, the production and destruction rates of $HO_2$, $RO_2$, and total $RO_x$ radicals were very consistent, but a significant lack of a source term for OH radicals existed after 10:00. This missing source became more pronounced during the Heavy period, reaching 16 $ppb\ h^{-1}$ at noon, which is close to the results observed by APHH but 3 times that observed by Heshan in the PRD region (Tan et al., 2019b; Whalley et al., 2021). The ratio of OH production-to-destruction rate during the Semi II period was close to 1, indicating consistency between the observed results of OH, $HO_2$, $k_{OH}$, and other precursors (Whalley et al., 2018). However, the generation of $HO_2$ radicals in the morning was about twice as high as the removal rate, suggesting that there are contributions from unconsidered $HO_2$ radical removal chan-

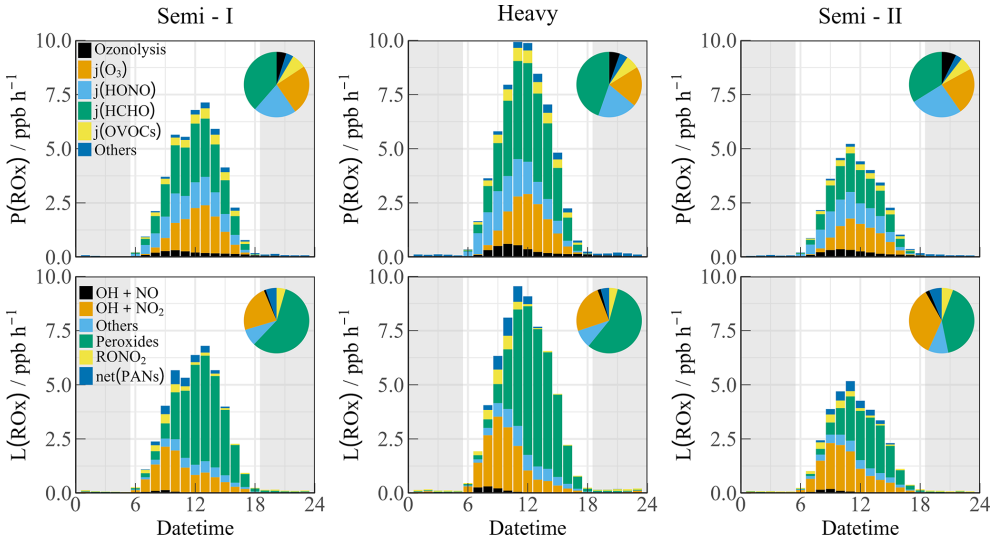


**Figure 5.** The diurnal profiles of $RO_x$ budget during different polluted episodes (Semi I, Heavy, and Semi II). The pie chart denotes proportions in different parts during the daytime (10:00–15:00). The grey areas denote nighttime.

nels (such as heterogeneous reactions) (Song et al., 2021). During the Heavy period, there was a rapid total removal rate of $RO_2$ radicals, reflecting the dominated $HO_2$ generation by the reaction of $RO_2$ radicals with NO. Although the $P(HO_2)$ and $D(HO_2)$ were quite in balance, the removal rate of $RO_2$ radicals far exceeded the known production rate (especially before 12:00). Previous work has shown that halogen chemistry (such as photolysis of nitryl chloride ($ClNO_2$)) could be an important source in the morning time, but this was not included in the calculation of $RO_x$ or $RO_2$ budget in this campaign (Tan et al., 2017b). The steady-state analysis for $HO_2$ radical in the London campaign emphasized that only by significantly reducing the observed $RO_2$-to-$HO_2$ propagation rate to just 15 % could balance both $P(HO_2)$ and $D(HO_2)$, indicating that the $RO_2$-related mechanism for propagation to other radical species may not be fully understood (Whalley et al., 2018). Therefore, the current knowledge seems unlikely to explain the required source–sink difference of nearly 25 ppb h$^{-1}$ in the $RO_2$ budget. Sensitivity analysis is needed to further infer the causes of the difference for the experimental budget analysis.

### 3.3 Oxidation comparison

The concentration of OH radicals during the daytime is a crucial indicator of atmospheric oxidation levels (Liu et al., 2021). Table 2 summarized radicals and related parameters for regions with similar latitudes (32.0° ± 2° N, $j(O^1D)$ ≈ 2.5 ± 0.5 × 10$^{-5}$ s$^{-1}$). The joint influence of solar radiation and local photochemistry resulted in megacities exhibiting intense oxidation levels in summer/autumn, characterized by OH radicals being maintained at approximately 10.0 × 10$^6$ cm$^{-3}$ at noon. Notably, an observation in Houston revealed an OH concentration of nearly 20.0 × 10$^6$ cm$^{-3}$, with $k_{OH}$ of 10 s$^{-1}$ (Mao et al., 2010). In areas such as Los Angeles, Pasadena, and Tokyo, the propagation efficiency of radicals was restricted due to fresh anthropogenic emissions. OH concentrations were only half of those observed in other megacities, with higher inorganic-dominated $k_{OH}$ recorded (Pasadena, ∼ 20 s$^{-1}$) (George et al., 1999; Griffith et al., 2016; Kanaya et al., 2007b). In the TROPSTECT observation, the observed $k_{OH}$ exceeded the mean value at the same latitude (> 15 s$^{-1}$). Additionally, during the Heavy episode, higher OH concentration (13.5 × 10$^6$ cm$^{-3}$) was found, comparable to the highest level at regions with similar latitude (Houston 2000/2006, (Mao et al., 2010)). Synchronous elevation in radical concentration and reactivity indicated a strong oxidation level in the YRD region.

The observations in the YRD region showed a stable conversion factor (OH-$j(O^1D)$) of 4 ± 1 × 10$^{11}$ cm$^{-3}$ s, which was comparable to other megacities in the PRD, NCP, and SCB regions (Ma et al., 2022; Tan et al., 2019a). The corresponding slope between OH concentration and solar radiation was used to quantify the oxidation efficiency from photolysis, and it was observed that a higher slope of 5.3 × 10$^{11}$ cm$^{-3}$ s during the Heavy period indicated an active radical chemistry. This implies that there is a strong oxidation efficiency from photolysis in the YRD region.

During summer and autumn seasons, photochemical pollution is a common occurrence, as noted by Tan et al. (2021). Analysis of radical concentration across different regions reveals that the YRD region exhibited concentrations higher than 10$^7$ cm$^{-3}$, slightly lower than in Guangzhou in 2006 but consistent with observations in other megacities (Ma et al., 2022; Tan et al., 2017a; Lu et al., 2012; Yang et al., 2021a). Conversely, winter is characterized by haze pollution (Ma et al., 2019). An urban site in Shanghai reported

**Table 2.** Summary of radical concentrations and related species concentrations at regions with similar latitude and megapolitan areas in China. All data are listed as the average in noontime (11:00–13:00).

| Location | Latitude | Year | OH ($10^6$ cm$^{-3}$) | $k_{OH}$ ($s^{-1}$) | $j(O^1D)$ ($10^{-5}$ $s^{-1}$) | Slope ($10^{11}$ cm$^{-3}$ s) | References |
|---|---|---|---|---|---|---|---|
| Regions with similar latitude | | | | | | | |
| Los Angeles | 34.1° N | Sep 1993 | 6.0 | – | – | – | George et al. (1999) |
| Nashville | 36.2° N | Jun–Jul 1999 | 10.0 | 10.2 | 3.0 | 3.3[c] | Martinez et al. (2003) |
| Houston | 29.7° N | Aug 2000 | 20.0 | 9.0[b] | 3.0 | 6.7[c] | Mao et al., 2010) |
| Tokyo | 35.6° N | Jul–Aug 2004 | 6.3 | – | 2.5 | 3.0 | Kanaya et al. (2007a) |
| Houston | 29.7° N | Sep 2006 | 15.0 | 11.0 | 3.1 | 5.0[c] | Mao et al. (2010) |
| Pasadena | 34.1° N | May–Jun 2010 | 4.0 | 20.0 | 2.5 | 1.6[c] | Griffith et al. (2016) |
| Taizhou | 32.6° N | May–Jun 2018 | 10.6 | 10.8[a] | 2.1 | 4.8 | Ma et al. (2022) |
| Chengdu | 30.7° N | Aug 2019 | 10.0 | 8.0 | 2.2 | 4.1 | Yang et al. (2021a) |
| TROPSTECT (Heavy) | 31.9° N | Sep 2020 | 13.5 | 16.0 | 2.6 | 5.3 | This work |
| TROPSTECT (Semi) | 31.9° N | Sep 2020 | 7.2 | 14.2 | 2.4 | 3.1 | This work |
| Regions in megapolitan areas in China | | | | | | | |
| Guangzhou (PRD) | 23.5° N | Jul 2006 | 12.6 | 17.9 | 3.5[b] | 4.5 | Lu et al. (2012) |
| Wangdu (NCP) | 38.7°N | Jun–Jul 2014 | 8.3 | 15.0 | 1.8 | 4.5 | Tan et al. (2017b) |
| Beijing (NCP) | 39.9° N | May–Jun 2017 | 9.0 | 30.0 | 2.4 | 3.8[c] | Whalley et al. (2021) |
| Taizhou (YRD) | 32.6° N | May–Jun 2018 | 10.6 | 10.8[a] | 2.1 | 4.8 | Ma et al. (2022) |
| Shenzhen (PRD) | 22.6° N | Sep–Oct 2018 | 4.5 | 21.0 | 1.8 | 2.4 | Yang et al. (2022) |
| Chengdu (SCB) | 30.7° N | Aug 2019 | 9.0 | 8.0 | 2.2 | 4.0 | Yang et al. (2021a) |
| Hefei (YRD) | 31.9° N | Sep 2020 | 10.4 | 14.3 | 2.4 | 4.4 | This work |

[a] The modeled $k_{OH}$. [b] Value only in the afternoon. [c] Using the ratio of OH / $j(O^1D)$.

a peak OH concentration of $2.6 \times 10^6$ cm$^{-3}$, closely resembling the $1.7–3.1 \times 10^6$ cm$^{-3}$ range found in the polluted winter atmosphere (Zhang et al., 2022a). Although no significant regional disparities in oxidation levels were detected in agglomerations, attention should be directed to the YRD region due to its elevated radical concentration, reactivity, and photolysis efficiency, signaling the need to investigate its role in radical chemistry.

## 4 Discussion

### 4.1 Measurement–model reconciliation for radicals

#### 4.1.1 OH underestimation

A full suite of OH, $HO_2$, $RO_2$, and $k_{OH}$ measurements was utilized in the TROPSTECT campaign to untangle a thorough understanding of oxidation mechanisms where base model failed. One specific phenomenon was the absence of an OH source in situations where NO levels gradually decreased after 10:00. Missing OH sources are closely related to the chemistry of OVOCs (Yang et al., 2024a; Qu et al., 2021). Reactive aldehyde chemistry, particularly the autoxidation of carbonyl organic peroxy radicals ($R(CO)O_2$) derived from higher aldehydes, is a significant OH regeneration mechanism that has been shown to contribute importantly to OH sources in regions with abundant natural and anthropogenic emissions during warm seasons (Yang et al., 2024b). In this study, the Higher Aldehyde Mechanism (HAM) by Yang et al. (2024b) was parameterized into the base model to test new insights into the potential missing radical chemistry (Fig. 6). The results indicate that the contribution of HAM to OH radicals in different episodes ranged between 4.4 %–6.0 % (Fig. 6a). The addition of HAM seems to have a small effect on the measured OH radical concentration. Thus, an empirical hypothesis is proposed in the "HAM+4ALD on" scenario to increase the concentration of higher-order aldehydes by approximately 4-fold, thereby replicating the effect of missing OVOC sources on radicals. Detailed description is presented in Sect. 4.3.

#### 4.1.2 $RO_2$ underestimation

The base scenario in Semi II is capable of accurately reproducing the concentrations of OH and $HO_2$ radicals within the data uncertainty. However, the simulated $RO_2$ concentration by the base model is only $3.78 \times 10^8$ cm$^{-3}$, which does not align with the observed oxidation levels in YRD, indicating a clear discrepancy. This underestimation is similarly evident in the APHH observation in Beijing, as the highest observed concentration of $RO_2$ radicals reached $5.5 \times 10^9$ cm$^{-3}$, far exceeding the level predicted by MCM v3.3.1 (Whalley et al., 2021). The failure to reproduce the $RO_2$ concentration reflects the inadequacy of the mechanisms related to $RO_2$ radicals due to diverse oxidation reactions. This issue is further elucidated by previous studies, which highlighted the

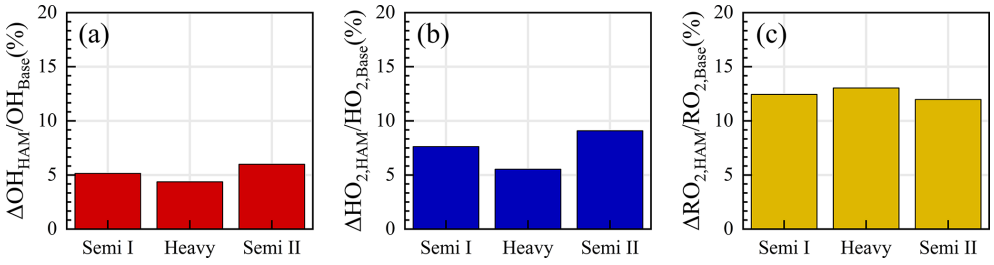


**Figure 6.** The response of **(a)** OH, **(b)** $HO_2$, and **(c)** $RO_2$ radicals to the Higher Aldehyde Mechanism (HAM) in different episodes (Semi I, Heavy, and Semi II) in diurnal time (10:00–15:00).

possibility of certain VOCs undergoing more intricate isomerization or fragmentation steps to sustain the long lifetime of $RO_2$ radicals (Whalley et al., 2018; Whalley et al., 2021). Higher aldehyde chemistry is a concrete manifestation of verifying the aforementioned hypothesis for $RO_2$ sources (Yang et al., 2024b). The autoxidation process of $R(CO)O_2$ encompasses a hydrogen migration process that transforms it into the •OOR(CO)OOH radical (Wang et al., 2019b). This radical subsequently reacts with NO to yield the •OR(CO)OOH radical. The •OR(CO)OOH radical predominantly undergoes two successive rapid hydrogen migration reactions, ultimately resulting in the formation of $HO_2$ radicals and hydroperoxy carbonyl (HPC). Consequently, HAM extends the lifetime of the $RO_2$ radical, providing a valuable complement to the unaccounted sources of $RO_2$ radicals. As depicted in Fig. 6, the incorporation of HAM results in an approximate 7.4 % and 12.5 % increase in the concentrations of $HO_2$ and $RO_2$ radicals, respectively.

It is important to note that the total concentrations of primary emitted aldehydes and the HPC group may be underestimated, which could lead to the aforementioned analysis being conservative in nature. The union of $k_{OH}$ and $RO_2$ measurement can help reveal the magnitude of missing $RO_2$ as a hypothesis of sensitivity analysis. Discrepancy of OH reactivity ($\sim$ 3–5 $s^{-1}$) between measurement and model suggested that an additional driving force was necessary to complete the OH to $RO_2$ step. Additional monoterpene species (MTS) were employed to represent the complex isomerization steps experienced by $RO_2$ radicals derived from other unmeasured VOCs. In the "HAM+4ALD+MTS" scenario, approximately 0.4 ppb of monoterpenes is introduced to represent the reactive BVOCs. The 0.4 ppb monoterpene level aligns with another observation from the EXPLORE-2018 campaign conducted in a suburban environment of the YRD region and can better reconcile the missing $k_{OH}$ between observation and simulation (Fig. 7) (Wang et al., 2022b). RACM2 identified $\alpha$-pinene (API) and limonene (LIM) as being representative of monoterpenes, and the mean of the species was considered the average effect of monoterpenes chemistry (the green line in Fig. 7). The "HAM+4ALD+MTS on" scenario can reasonably reproduce the measured reactivity, and the chemistry of peroxy radicals in Semi II was reasonably described by introducing the source of complex alkoxy radicals, decreasing the observed-to-modeled ratio from 2.2 to 1.3. Furthermore, the introduction of additional complex alkoxy radicals had a minimal impact on $HO_x$ chemistry, with changes in daytime OH and $HO_2$ concentrations of less than $5 \times 10^5$ and $2.5 \times 10^7$ $cm^{-3}$, respectively. This demonstrates the robustness of the $HO_x$ radical in response to potential monoterpene.

### 4.2 Effect of mechanism reconciliation on oxidation

Upon completing the hypothetical investigation into the radical underestimation, both radical concentration and oxidation coordinating deficiency are worth being examined (Fig. S8). To eliminate the influence of non-photolytic processes, only the daytime concentration range with $j(O^1D)$ greater than $5 \times 10^{-6}$ $s^{-1}$ was selected. The box plots illustrate the ratio of observation to simulation (base model), with the circles representing the average values after integrating different mechanisms into the base scenario. In the low NO regime (NO < 1 ppb), the OH underestimation was consistently prominent as NO concentration decreased, and the base model was able to reasonably reflect the $HO_2$ distribution. As NO levels increased, the simulated OH concentration aligned well with the observation, but both $HO_2$ and $RO_2$ concentrations exhibited underprediction. $RO_2$ underestimation extended across the entire NO range and could rise to over 10 times when NO levels reached about 10 ppb. Sensitivity tests based on the full suite of radical measurements revealed that the introduction of larger $RO_2$ alleviated the absence of certain sources by 2 to 4 times.

The coordinate ratios of radical serves as another test for $RO_x$ propagation (Fig. 8). The observed $HO_2$ / OH ratio is approximately 100, declining to some extent as the concentration of NO increases, which is consistent with previous studies (Griffith et al., 2016; Griffith et al., 2013). However, the base model does not accurately replicate the curve depicting the change in $HO_2$ / OH ratio, as shown in Fig. 8a. At low NO levels, the ratio is significantly overestimated and shows a steeper decline compared to the base scenario as NO levels increase. Furthermore, the observed $RO_2$ / OH ratios remain around 100, whereas the predicted values are significantly

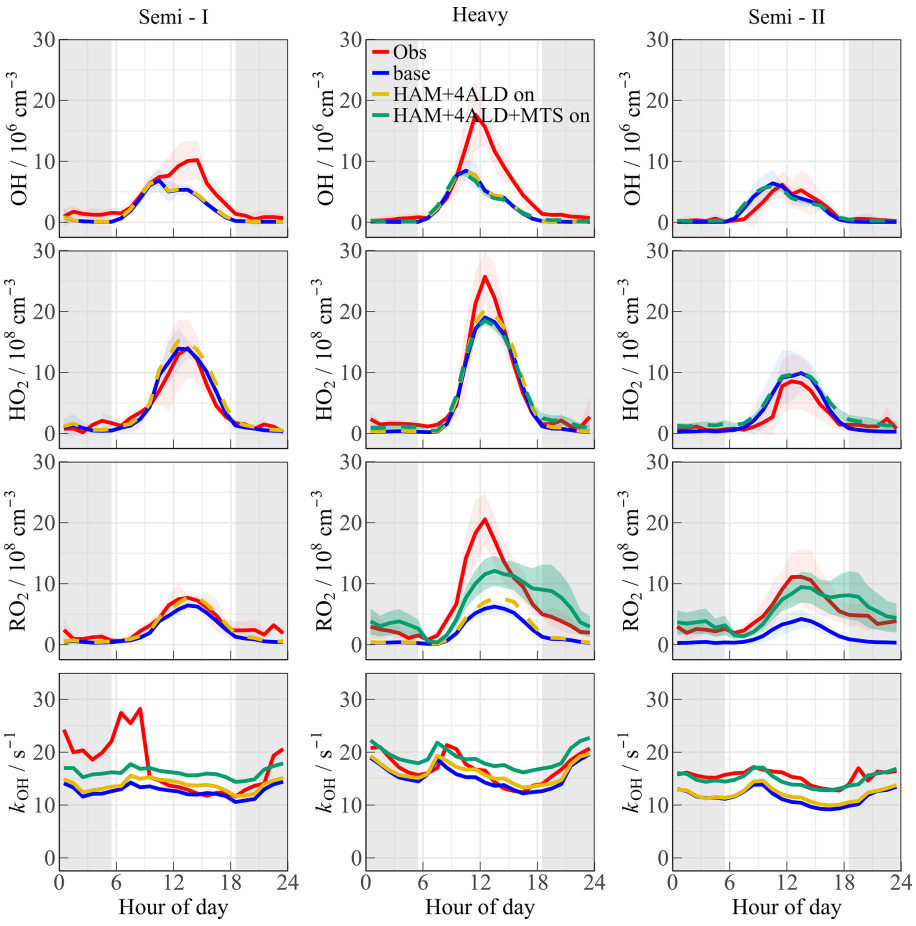


**Figure 7.** The mean diurnal profiles of measured and modeled OH, $HO_2$, $RO_2$, and $k_{OH}$ at different scenarios. Among them, the red, blue, and dotted yellow lines represent the observed values, simulated values under base model and "HAM+4ALD" scenario, respectively. The green line and its shaded area represent the results under the HAM+4ALD+MTS scenario. The grey areas denote nighttime.

underestimated when NO exceeds 1 ppb (refer to Fig. 8b). In terms of the observed $HO_2$ / $RO_2$ ratio, it maintains a relatively constant trend within the range of 0.5–1.5, while the model overestimated by more than 2 times, highlighting an inconsistency between the conversion of $RO_2 \rightarrow HO_2$. The incorporation of HAM has proven to slightly balance the $HO_2$ / OH ratio as illustrated in Fig. 8a and altered the coordination between $RO_2$ and OH across the entire NO range (Fig. 8b). The larger $RO_2$ isomerization associated with HAM in chemically complex environments is key to fully understanding tropospheric chemistry, and a better coordination of $HO_2$ / OH, $RO_2$ / OH, and $HO_2$ / $RO_2$ ratios is established by incorporating additional mechanisms.

The $HO_2$ / $RO_2$ parameter was utilized to explore the transformation relationship between $HO_2$ and $RO_2$ radicals. If $HO_2$ is formed from an $RO_2$ radical, it would result in an $HO_2$ / $RO_2$ radical concentration ratio of approximately 1. The $HO_2$ / $RO_2$ ratios derived from radical concentrations measured by laser-induced fluorescence instruments and calculated using the MCM or RACM models were summarized in Fig. 9. In field studies, the observed $HO_2$ / $RO_2$ ratios were between 0.2–1.7 under low NO conditions (NO < 1 ppb) and only 0.1–0.8 under high NO conditions (3 < NO < 6 ppb). From the perspective of model–observation matching, except for three measurements in ClearfLo, ICOZA, and APHH-summer campaigns, the $HO_2$ / $RO_2$ ratios in other regions could be reasonably reflected by the MCM or RACM2 (Woodward-Massey et al., 2023; Whalley et al., 2021; Whalley et al., 2018; Färber et al., 2024). However, the ratio is generally underestimated under high NO conditions, reaching up to 5 times in ClearfLo. According to the latest chamber experiments, the $HO_2$ / $RO_2$ radical concentration ratios for VOCs forming $HO_2$ are 0.6 for both one-step and two-step reactions. Therefore, the extremely low $HO_2$ / $RO_2$ ratios observed in field campaigns can only be explained if almost all $RO_2$ radicals undergo multiple-step reactions before forming $HO_2$. During the TROPSTECT campaign, the observed $HO_2$ / $RO_2$ remains at 1.1 and 0.8 under low NO and high NO conditions, respectively. After considering the sources of complex alkoxy radicals in the HAM+4ALD+MTS on

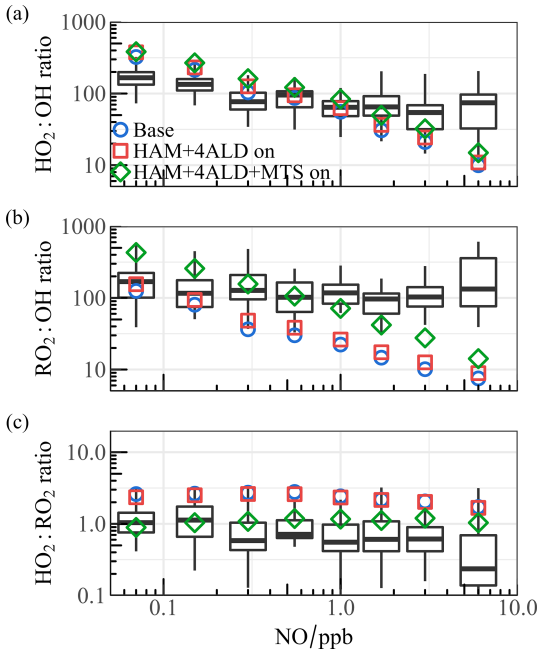


**Figure 8.** The ratios for **(a)** $HO_2$ / OH, **(b)** $RO_2$ / OH, and **(c)** $HO_2$ / $RO_2$ show a correlation with NO levels. Box plot diagrams are used to illustrate the minimum, 25th percentile, median, 75th percentile, and maximum values of the observed dataset. The point styles (circular, square, diamond-shaped) represent the median values for the base model as well as for different mechanisms added to the model within various ranges.

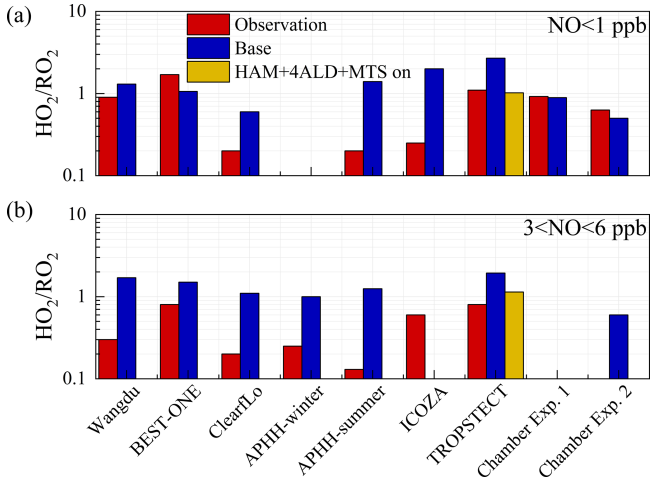


**Figure 9.** Summary of the $HO_2$ / $RO_2$ ratios derived from radical concentrations measured by laser-induced fluorescence instruments and calculated using the MCM or RACM models under **(a)** low NO and **(b)** high NO conditions. Chamber Exp. 1 and Chamber Exp. 2 denote the parameters by single-step $HO_2$ formation and multi-step $HO_2$ formation determined in the chamber by Färber et al. (2024).

scenario, the simulated values of $HO_2$ / $RO_2$ in both low NO and high NO regions match the observed values well.

### 4.3 Missing OVOC sources influence ozone production

The consistency between model predictions and observed measurements for ozone production, akin to the concentration ratio of $HO_2$ / $RO_2$, is depicted in Fig. 10a and b. In areas with low NO levels, the ratio of modeled to actual ozone production ranges from 0.5 to 2, with the exception of the ClearfLo and APHH-summer datasets (Woodward-Massey et al., 2023; Whalley et al., 2021). Conversely, under high NO conditions (with NO concentrations between 3 and 6 ppbv), the ozone production rate ($P(O_x)$) derived from measured radical concentrations typically exceeds that of the base model's predictions by more than threefold. Laboratory experiments focusing on the oxidation of representative VOCs suggest that ozone production can be enhanced by approximately 25 % for the anthropogenic VOCs under investigation (Färber et al., 2024).

The reasons for the discrepancy between simulated and observed values for ozone production deserve further investigation. As depicted in Fig. 10c, the simulated $HO_2$ / $RO_2$ ratios display a robust positive correlation with photochemical activity, fluctuating between 2 and 4. A notable feature during severe ozone pollution is the intense distribution of formaldehyde, with an average concentration of $21.81 \pm 4.57$ ppb (11:00–13:00). While formaldehyde acts as a precursor for $HO_2$ radicals, it does not directly generate $RO_2$ radicals. The contributions of OVOCs to the $RO_x$ radical do not exhibit the same intensity as formaldehyde, and the current mechanism encounters difficulties in replicating formaldehyde concentrations (Fig. S9). The simulation of formaldehyde concentrations using MCM v3.3.1 has shown improvement, indicating that the secondary formation of unmeasured species, such as OVOCs, will feed back on $RO_2$ radical levels. When formaldehyde levels are unconstrained, the simulated $HO_2$ / $RO_2$ ratios align with observations, suggesting that under the prevailing chemical mechanism, the photochemical efficiency of formaldehyde and other OVOCs is similar. Therefore, an empirical hypothesis is proposed to amplify the concentration of higher-order aldehydes by a factor of about 4, which is the proportion of formaldehyde concentration underestimated by the model. The qualitative assessment of the impact of missing aldehyde primary emissions on $RO_2$ radical concentrations was combined with HAM across the entire photochemical spectrum (Fig. S10). An enhanced impact of aldehyde autoxidation in the presence of weak photochemical conditions could alter the simulated levels of OH and $HO_2$ radicals by approximately 13.9 % and 18.1 %, respectively. However, higher ALD concentrations will be achieved under intensive photochemical conditions, leading to the gradual dominance of the sink channels for OH + OVOCs, with the effect of autoxidation mechanisms gradually decreasing. $RO_2$ radical concentrations are notably more sensitive to HAM, where additional incorporated OVOCs can enhance the simulation of $RO_2$ radical concentrations by 20 %–40 %.

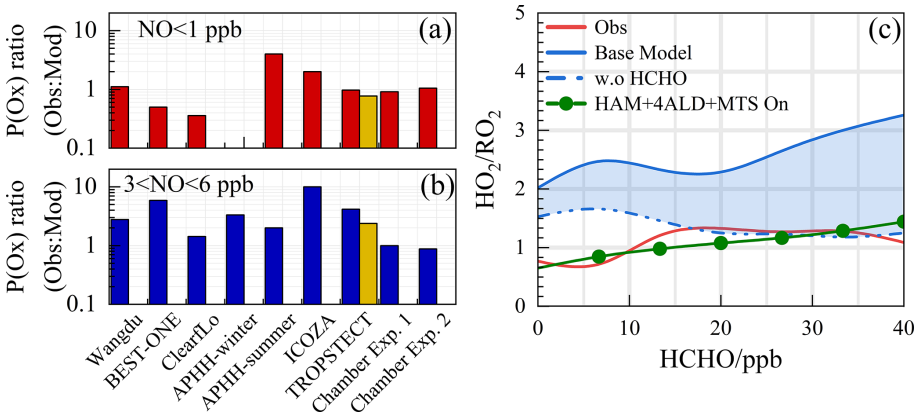


**Figure 10.** Summary of the $P(O_x)_{Obs}$ / $P(O_x)_{Mod}$ under **(a)** low NO and **(b)** high NO conditions. The yellow bar chart represents the simulation scenario of HAM+4ALD+MTS on. **(c)** The ratios for $HO_2$ / $RO_2$ show a correlation with HCHO levels. The blue shading represents the range of variation from constrained to unconstrained formaldehyde conditions. Chamber Exp. 1 and Chamber Exp. 2 denote the parameters by single-step $HO_2$ formation and multi-step $HO_2$ formation determined in the chamber by Färber et al. (2024).

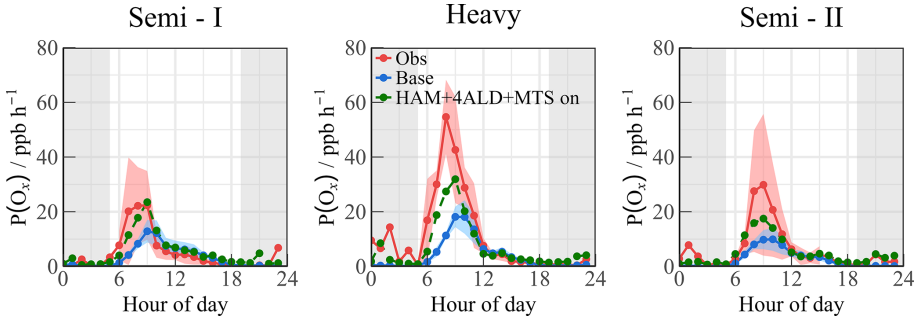


**Figure 11.** The $P(O_x)$ values that calculated by radical values under different scenarios. The grey areas denote nighttime.

On the basis of HAM, the HAM+4ALD+MTS on scenario represents an effort to enhance the congruence between modeled and measured radical concentrations. In Fig. S11, with increasing NO concentration, the overall $P(O_x)$ was amplified, reaching a maximum of approximately 30 ppb $h^{-1}$. However, the imperfect understanding of the mechanisms related to peroxy radicals ultimately leads to misjudgment of the ozone production process in high NO regimes, with a degree of underestimation close to 10 times, as illustrated in Fig. S11b. Notably, the deficiency in the ozone generation mechanism was adequately explained within a certain range in the HAM +4ALD+MTS on scenario, leading to an enhancement in the simulation performance of $P(O_x)$ in the high $NO_x$ region. The incorporation of OVOCs and larger alkoxy radicals derived from monoterpenes has refined the model–measurement agreement for ozone formation under high NO conditions, reducing the discrepancy from 4.17 to 2.39 (Fig. 11).

Therefore, reasonable simulation of the concentration of peroxy radicals is key to accurately quantifying the process of ozone generation. Although limiting formaldehyde can partially offset the $HO_2$ radical cycle and enhance the precision of $HO_x$ radical chemistry studies, additional measurements should be undertaken for other OVOCs, coupled with the deployment of full-chain radical detection systems, to accurately elucidate the oxidation processes under severe ozone pollution conditions.

## 5 Conclusion

The full suite of radical measurements of OH, $HO_2$, $RO_2$, and $k_{OH}$ was first deployed in the YRD region (TROPSTECT) and encountered with a prolonged ozone pollution in September 2020. The diurnal peaks of radicals exhibited considerable variation due to environmental factors, showing ranges of 3.6 to 27.1 $\times$ $10^6$ $cm^{-3}$ for OH, 2.1 to 33.2 $\times$ $10^8$ $cm^{-3}$ for $HO_2$, and 4.9 to 30.5 $\times$ $10^8$ $cm^{-3}$ for $RO_2$. Continuous $k_{OH}$ data fell within a range of 8.6–30.2 $s^{-1}$, demonstrating the dominant behavior of organic species in diurnal reactivity. Furthermore, observations in the YRD region were found to be similar to those in other megacities, suggesting no significant regional differences in oxidation levels were observed in agglomerations overall.

In a heavy ozone pollution episode, the oxidation reached an intensive level compared with other sites, and the simulated OH, $HO_2$, and $RO_2$ radicals provided by RACM2-LIM1 failed to adequately match the observed data in terms of both radical concentration and experimental radical budget. Sensitivity tests based on the full suite of radical measurement revealed that HAM effectively complements the non-traditional regeneration of OH radicals, improving by 4.4 %–6.0 % compared to the base scenario, while the concentrations of $HO_2$ and $RO_2$ radicals increased by approximately 7.4 % and 12.5 %, respectively. Under the constraints of $k_{OH}$ measurement, the inclusion of OVOCs and larger alkoxy radicals derived from monoterpenes enabled better coordination of $HO_2$ / OH, $RO_2$ / OH, and $HO_2$ / $RO_2$ ratios and adequately improved the model–measurement consistency for ozone formation, reducing the discrepancy under high NO conditions from 4.17 to 2.39. This study enabled a deeper understanding of the tropospheric radical chemistry at play. The following two points were notable:

- A full suite of radical measurements can bridge the gap as the base model in more chemically complex environments as a hypothesis of sensitivity tests.
- Additional measurements targeting more OVOCs should also be conducted to fulfill the $RO_2$-related imbalance and then accurately elucidate the oxidation under severe ozone pollution.

**Data availability.** The data used in this study are available upon request (rzhu@aiofm.ac.cn).

**Supplement.** The supplement related to this article is available online at https://doi.org/10.5194/acp-25-3011-2025-supplement.

**Author contributions.** WQL, PHX, and RZH contributed to the conception of this study. RZH and GXZ performed the data analyses and manuscript writing. All authors contributed to measurements, discussed results, and commented on the paper.

**Competing interests.** The contact author has declared that none of the authors has any competing interests.

**Disclaimer.** Publisher's note: Copernicus Publications remains neutral with regard to jurisdictional claims made in the text, published maps, institutional affiliations, or any other geographical representation in this paper. While Copernicus Publications makes every effort to include appropriate place names, the final responsibility lies with the authors.

**Acknowledgements.** The authors appreciate the valuable comments from three anonymous reviewers.

**Financial support.** This work was supported by the National Key R&D Program of China (grant no. 2022YFC3700301), the National Natural Science Foundation of China (grant nos. 62275250, U19A2044, 42030609), the Natural Science Foundation of Anhui Province (grant no. 2008085J20), the Anhui Provincial Key R&D Program (grant no. 2022l07020022), and the Distinguished Program of Jianghuai Talents Program of Excellence (HYRC-STZ202401).

**Review statement.** This paper was edited by Eleanor Browne and reviewed by three anonymous referees.

## References

Duan, J., Qin, M., Ouyang, B., Fang, W., Li, X., Lu, K., Tang, K., Liang, S., Meng, F., Hu, Z., Xie, P., Liu, W., and Häsler, R.: Development of an incoherent broadband cavity-enhanced absorption spectrometer for in situ measurements of HONO and $NO_2$, Atmos. Meas. Tech., 11, 4531–4543, https://doi.org/10.5194/amt-11-4531-2018, 2018.

Färber, M., Fuchs, H., Bohn, B., Carlsson, P. T. M., Gkatzelis, G. I., Marcillo Lara, A. C., Rohrer, F., Vereecken, L., Wedel, S., Wahner, A., and Novelli, A.: Effect of the Alkoxy Radical Chemistry on the Ozone Formation from Anthropogenic Organic Compounds Investigated in Chamber Experiments, ACS ES&T Air, 1, 1096–1111, https://doi.org/10.1021/acsestair.4c00064, 2024.

Fuchs, H., Holland, F., and Hofzumahaus, A.: Measurement of tropospheric $RO_2$ and $HO_2$ radicals by a laser-induced fluorescence instrument, Rev. Sci. Instrum., 79, 084104, https://doi.org/10.1063/1.2968712, 2008.

George, L. A., Hard, T. M., and O'Brien, R. J.: Measurement of free radicals OH and $HO_2$ in Los Angeles smog, J. Geophys. Res.-Atmos., 104, 11643–11655, 1999.

Griffith, S. M., Hansen, R. F., Dusanter, S., Stevens, P. S., Alaghmand, M., Bertman, S. B., Carroll, M. A., Erickson, M., Galloway, M., Grossberg, N., Hottle, J., Hou, J., Jobson, B. T., Kammrath, A., Keutsch, F. N., Lefer, B. L., Mielke, L. H., O'Brien, A., Shepson, P. B., Thurlow, M., Wallace, W., Zhang, N., and Zhou, X. L.: OH and $HO_2$ radical chemistry during PROPHET 2008 and CABINEX 2009 – Part 1: Measurements and model comparison, Atmos. Chem. Phys., 13, 5403–5423, https://doi.org/10.5194/acp-13-5403-2013, 2013.

Griffith, S. M., Hansen, R. F., Dusanter, S., Michoud, V., Gilman, J. B., Kuster, W. C., Veres, P. R., Graus, M., de Gouw, J. A., Roberts, J., Young, C., Washenfelder, R., Brown, S. S., Thalman, R., Waxman, E., Volkamer, R., Tsai, C., Stutz, J., Flynn, J. H., Grossberg, N., Lefer, B., Alvarez, S. L., Rappenglueck, B., Mielke, L. H., Osthoff, H. D., and Stevens, P. S.: Measurements of hydroxyl and hydroperoxy radicals during CalNex-LA: Model comparisons and radical budgets, J. Geophys. Res.-Atmos., 121, 4211–4232, https://doi.org/10.1002/2015jd024358, 2016.

Heard, D. E. and Pilling, M. J.: Measurement of OH and $HO_2$ in the troposphere, Chem. Rev., 103, 5163–5198, https://doi.org/10.1021/cr020522s, 2003.

Hofzumahaus, A., Rohrer, F., Lu, K., Bohn, B., Brauers, T., Chang, C.-C., Fuchs, H., Holland, F., Kita, K., Kondo, Y., Li, X., Lou, S., Shao, M., Zeng, L., Wahner, A., and Zhang, Y.: Amplified Trace Gas Removal in the Troposphere, Science, 324, 1702–1704, https://doi.org/10.1126/science.1164566, 2009.

Hu, B., Duan, J., Hong, Y., Xu, L., Li, M., Bian, Y., Qin, M., Fang, W., Xie, P., and Chen, J.: Exploration of the atmospheric chemistry of nitrous acid in a coastal city of southeastern China: results from measurements across four seasons, Atmos. Chem. Phys., 22, 371–393, https://doi.org/10.5194/acp-22-371-2022, 2022.

Huang, J., Pan, X., Guo, X., and Li, G.: Health impact of China's Air Pollution Prevention and Control Action Plan: an analysis of national air quality monitoring and mortality data, Lancet Planet Health, 2, e313–e323, https://doi.org/10.1016/S2542-5196(18)30141-4, 2018.

Huang, X., Ding, A., Wang, Z., Ding, K., Gao, J., Chai, F., and Fu, C.: Amplified transboundary transport of haze by aerosol–boundary layer interaction in China, Nat. Geosci., 13, 428–434, https://doi.org/10.1038/s41561-020-0583-4, 2020.

Jenkin, M. E., Saunders, S. M., and Pilling, M. J.: The tropospheric degradation of volatile organic compounds: A protocol for mechanism development, Atmos. Environ., 31, 81–104, https://doi.org/10.1016/s1352-2310(96)00105-7, 1997.

Jenkin, M. E., Saunders, S. M., Wagner, V., and Pilling, M. J.: Protocol for the development of the Master Chemical Mechanism, MCM v3 (Part B): tropospheric degradation of aromatic volatile organic compounds, Atmos. Chem. Phys., 3, 181–193, https://doi.org/10.5194/acp-3-181-2003, 2003.

Jia, W., Zhang, X., and Wang, Y.: Assessing the pollutant evolution mechanisms of heavy pollution episodes in the Yangtze-Huaihe valley: A multiscale perspective, Atmos. Environ., 244, 117986, https://doi.org/10.1016/j.atmosenv.2020.117986, 2021.

Kanaya, Y., Cao, R. Q., Akimoto, H., Fukuda, M., Komazaki, Y., Yokouchi, Y., Koike, M., Tanimoto, H., Takegawa, N., and Kondo, Y.: Urban photochemistry in central Tokyo: 1. Observed and modeled OH and $HO_2$ radical concentrations during the winter and summer of 2004, J. Geophys. Res.-Atmos., 112, D21312, https://doi.org/10.1029/2007jd008670, 2007a.

Kanaya, Y. G., Cao, R. Q., Kato, S. G., Miyakawa, Y. K., Kajii, Y., Tanimoto, H., Yokouchi, Y., Mochida, M., Kawamura, K., and Akimoto, H.: Chemistry of OH and $HO_2$ radicals observed at Rishiri Island, Japan, in September 2003: Missing daytime sink of $HO_2$ and positive nighttime correlations with monoterpenes, J. Geophys. Res.-Atmos., 112, D11308, https://doi.org/10.1029/2006jd007987, 2007b.

Kanaya, Y., Hofzumahaus, A., Dorn, H.-P., Brauers, T., Fuchs, H., Holland, F., Rohrer, F., Bohn, B., Tillmann, R., Wegener, R., Wahner, A., Kajii, Y., Miyamoto, K., Nishida, S., Watanabe, K., Yoshino, A., Kubistin, D., Martinez, M., Rudolf, M., Harder, H., Berresheim, H., Elste, T., Plass-Dülmer, C., Stange, G., Kleffmann, J., Elshorbany, Y., and Schurath, U.: Comparisons of observed and modeled OH and $HO_2$ concentrations during the ambient measurement period of the $HO_x$Comp field campaign, Atmos. Chem. Phys., 12, 2567–2585, https://doi.org/10.5194/acp-12-2567-2012, 2012.

Levy, H.: Normal Atmosphere: Large Radical and Formaldehyde Concentrations Predicted, Science, 173, 141–143, https://doi.org/10.1126/science.173.3992.141, 1971.

Li, S., Lu, K., Ma, X., Yang, X., Chen, S., and Zhang, Y.: Field measurement of the organic peroxy radicals by the low-pressure reactor plus laser-induced fluorescence spectroscopy, Chinese Chem. Lett., 31, 2799–2802, https://doi.org/10.1016/j.cclet.2020.07.051, 2020.

Liu, S., Li, X., Shen, X., Zeng, L., Huang, X., Zhu, B., Lin, L., and Lou, S.: Measurement and partition analysis of atmospheric OH reactivity in autumn in Shenzhen, Acta Scientiae Circumstantiae, 39, 3600–3610, 2019.

Liu, Y., Li, J., Ma, Y., Zhou, M., Tan, Z., Zeng, L., Lu, K., and Zhang, Y.: A review of gas-phase chemical mechanisms commonly used in atmospheric chemistry modelling, J. Environ. Sci., 123, 522–534, https://doi.org/10.1016/j.jes.2022.10.031, 2022.

Liu, Z., Wang, Y., Hu, B., Lu, K., Tang, G., Ji, D., Yang, X., Gao, W., Xie, Y., Liu, J., Yao, D., Yang, Y., and Zhang, Y.: Elucidating the quantitative characterization of atmospheric oxidation capacity in Beijing, China, Sci. Total Environ., 771, 145306, https://doi.org/10.1016/j.scitotenv.2021.145306, 2021.

Lou, S., Holland, F., Rohrer, F., Lu, K., Bohn, B., Brauers, T., Chang, C. C., Fuchs, H., Häseler, R., Kita, K., Kondo, Y., Li, X., Shao, M., Zeng, L., Wahner, A., Zhang, Y., Wang, W., and Hofzumahaus, A.: Atmospheric OH reactivities in the Pearl River Delta – China in summer 2006: measurement and model results, Atmos. Chem. Phys., 10, 11243–11260, https://doi.org/10.5194/acp-10-11243-2010, 2010.

Lu, K., Guo, S., Tan, Z., Wang, H., Shang, D., Liu, Y., Li, X., Wu, Z., Hu, M., and Zhang, Y.: Exploring atmospheric free-radical chemistry in China: the self-cleansing capacity and the formation of secondary air pollution, Nat. Sci. Rev., 6, 579–594, https://doi.org/10.1093/nsr/nwy073, 2019.

Lu, K. D., Rohrer, F., Holland, F., Fuchs, H., Bohn, B., Brauers, T., Chang, C. C., Häseler, R., Hu, M., Kita, K., Kondo, Y., Li, X., Lou, S. R., Nehr, S., Shao, M., Zeng, L. M., Wahner, A., Zhang, Y. H., and Hofzumahaus, A.: Observation and modelling of OH and $HO_2$ concentrations in the Pearl River Delta 2006: a missing OH source in a VOC rich atmosphere, Atmos. Chem. Phys., 12, 1541–1569, https://doi.org/10.5194/acp-12-1541-2012, 2012.

Ma, X., Tan, Z., Lu, K., Yang, X., Chen, X., Wang, H., Chen, S., Fang, X., Li, S., Li, X., Liu, J., Liu, Y., Lou, S., Qiu, W., Wang, H., Zeng, L., and Zhang, Y.: OH and $HO_2$ radical chemistry at a suburban site during the EXPLORE-YRD campaign in 2018, Atmos. Chem. Phys., 22, 7005–7028, https://doi.org/10.5194/acp-22-7005-2022, 2022.

Ma, X. F., Tan, Z. F., Lu, K. D., Yang, X. P., Liu, Y. H., Li, S. L., Li, X., Chen, S. Y., Novelli, A., Cho, C. M., Zeng, L. M., Wahner, A., and Zhang, Y. H.: Winter photochemistry in Beijing: Observation and model simulation of OH and $HO_2$ radicals at an urban site, Sci. Total Environ., 685, 85–95, https://doi.org/10.1016/j.scitotenv.2019.05.329, 2019.

Mao, J., Ren, X., Chen, S., Brune, W. H., Chen, Z., Martinez, M., Harder, H., Lefer, B., Rappenglück, B., Flynn, J., and Leuchner, M.: Atmospheric oxidation capacity in the summer of Houston 2006: Comparison with summer measurements in other metropolitan studies, Atmos. Environ., 44, 4107–4115, https://doi.org/10.1016/j.atmosenv.2009.01.013, 2010.

Martinez, M., Harder, H., Kovacs, T. A., Simpas, J. B., Bassis, J., Lesher, R., Brune, W. H., Frost, G. J., Williams, E. J., Stroud, C. A., Jobson, B. T., Roberts, J. M., Hall, S. R., Shetter, R. E., Wert, B., Fried, A., Alicke, B., Stutz, J., Young, V. L., White, A. B., and Zamora, R. J.: OH and $HO_2$ concentrations, sources, and loss rates during the Southern Oxidants Study in Nashville, Tennessee, summer 1999, J. Geophys. Res.-Atmos., 108, 4617, https://doi.org/10.1029/2003jd003551, 2003.

Peeters, J., Muller, J. F., Stavrakou, T., and Nguyen, V. S.: Hydroxyl Radical Recycling in Isoprene Oxidation Driven by Hydrogen Bonding and Hydrogen Tunneling: The Upgraded LIM1 Mechanism, J. Phys. Chem. A, 118, 8625–8643, https://doi.org/10.1021/jp5033146, 2014.

Qu, H., Wang, Y., Zhang, R., Liu, X., Huey, L. G., Sjostedt, S., Zeng, L., Lu, K., Wu, Y., Shao, M., Hu, M., Tan, Z., Fuchs, H., Broch, S., Wahner, A., Zhu, T., and Zhang, Y.: Chemical Production of Oxygenated Volatile Organic Compounds Strongly Enhances Boundary-Layer Oxidation Chemistry and Ozone Production, Environ. Sci. Technol., 55, 13718–13727, https://doi.org/10.1021/acs.est.1c04489, 2021.

Ren, X., Olson, J. R., Crawford, J. H., Brune, W. H., Mao, J., Long, R. B., Chen, Z., Chen, G., Avery, M. A., Sachse, G. W., Barrick, J. D., Diskin, G. S., Huey, L. G., Fried, A., Cohen, R. C., Heikes, B., Wennberg, P. O., Singh, H. B., Blake, D. R., and Shetter, R. E.: $HO_x$ chemistry during INTEX-A 2004: Observation, model calculation, and comparison with previous studies, J. Geophys. Res.-Atmos., 113, D05310, https://doi.org/10.1029/2007jd009166, 2008.

Rohrer, F., Lu, K., Hofzumahaus, A., Bohn, B., Brauers, T., Chang, C.-C., Fuchs, H., Haeseler, R., Holland, F., Hu, M., Kita, K., Kondo, Y., Li, X., Lou, S., Oebel, A., Shao, M., Zeng, L., Zhu, T., Zhang, Y., and Wahner, A.: Maximum efficiency in the hydroxyl-radical-based self-cleansing of the troposphere, Nat. Geosci., 7, 559–563, https://doi.org/10.1038/ngeo2199, 2014.

Shi, X., Ge, Y., Zheng, J., Ma, Y., Ren, X., and Zhang, Y.: Budget of nitrous acid and its impacts on atmospheric oxidative capacity at an urban site in the central Yangtze River Delta region of China, Atmos. Environ., 238, 117725, https://doi.org/10.1016/j.atmosenv.2020.117725, 2020.

Slater, E. J., Whalley, L. K., Woodward-Massey, R., Ye, C., Lee, J. D., Squires, F., Hopkins, J. R., Dunmore, R. E., Shaw, M., Hamilton, J. F., Lewis, A. C., Crilley, L. R., Kramer, L., Bloss, W., Vu, T., Sun, Y., Xu, W., Yue, S., Ren, L., Acton, W. J. F., Hewitt, C. N., Wang, X., Fu, P., and Heard, D. E.: Elevated levels of OH observed in haze events during wintertime in central Beijing, Atmos. Chem. Phys., 20, 14847–14871, https://doi.org/10.5194/acp-20-14847-2020, 2020.

Song, H., Lu, K., Dong, H., Tan, Z., Chen, S., Zeng, L., and Zhang, Y.: Reduced Aerosol Uptake of Hydroperoxyl Radical May Increase the Sensitivity of Ozone Production to Volatile Organic Compounds, Environ. Sci. Tech. Lett., 9, 22–29, https://doi.org/10.1021/acs.estlett.1c00893, 2021.

Stockwell, W. R., Kirchner, F., Kuhn, M., and Seefeld, S.: A new mechanism for regional atmospheric chemistry modeling, J. Geophys. Res.-Atmos., 102, 25847–25879, https://doi.org/10.1029/97jd00849, 1997.

Stone, D., Whalley, L. K., and Heard, D. E.: Tropospheric OH and $HO_2$ radicals: field measurements and model comparisons, Chem. Soc. Rev., 41, 6348–6404, https://doi.org/10.1039/c2cs35140d, 2012.

Tan, Z., Fuchs, H., Lu, K., Hofzumahaus, A., Bohn, B., Broch, S., Dong, H., Gomm, S., Häseler, R., He, L., Holland, F., Li, X., Liu, Y., Lu, S., Rohrer, F., Shao, M., Wang, B., Wang, M., Wu, Y., Zeng, L., Zhang, Y., Wahner, A., and Zhang, Y.: Radical chemistry at a rural site (Wangdu) in the North China Plain: observation and model calculations of OH, $HO_2$ and $RO_2$ radicals, Atmos. Chem. Phys., 17, 663–690, https://doi.org/10.5194/acp-17-663-2017, 2017a.

Tan, Z., Fuchs, H., Lu, K., Hofzumahaus, A., Bohn, B., Broch, S., Dong, H., Gomm, S., Häseler, R., He, L., Holland, F., Li, X., Liu, Y., Lu, S., Rohrer, F., Shao, M., Wang, B., Wang, M., Wu, Y., Zeng, L., Zhang, Y., Wahner, A., and Zhang, Y.: Radical chemistry at a rural site (Wangdu) in the North China Plain: observation and model calculations of OH, $HO_2$ and $RO_2$ radicals, Atmos. Chem. Phys., 17, 663–690, https://doi.org/10.5194/acp-17-663-2017, 2017b.

Tan, Z., Lu, K., Jiang, M., Su, R., Wang, H., Lou, S., Fu, Q., Zhai, C., Tan, Q., Yue, D., Chen, D., Wang, Z., Xie, S., Zeng, L., and Zhang, Y.: Daytime atmospheric oxidation capacity in four Chinese megacities during the photochemically polluted season: a case study based on box model simulation, Atmos. Chem. Phys., 19, 3493–3513, https://doi.org/10.5194/acp-19-3493-2019, 2019a.

Tan, Z., Lu, K., Hofzumahaus, A., Fuchs, H., Bohn, B., Holland, F., Liu, Y., Rohrer, F., Shao, M., Sun, K., Wu, Y., Zeng, L., Zhang, Y., Zou, Q., Kiendler-Scharr, A., Wahner, A., and Zhang, Y.: Experimental budgets of OH, $HO_2$, and $RO_2$ radicals and implications for ozone formation in the Pearl River Delta in China 2014, Atmos. Chem. Phys., 19, 7129–7150, https://doi.org/10.5194/acp-19-7129-2019, 2019b.

Tan, Z., Ma, X., Lu, K., Jiang, M., Zou, Q., Wang, H., Zeng, L., and Zhang, Y.: Direct evidence of local photochemical production driven ozone episode in Beijing: A case study, Sci. Total Environ., 800, 148868, https://doi.org/10.1016/j.scitotenv.2021.148868, 2021.

Tan, Z. F., Lu, K. D., Dong, H. B., Hu, M., Li, X., Liu, Y. H., Lu, S. H., Shao, M., Su, R., Wang, H. C., Wu, Y. S., Wahner, A., and Zhang, Y. H.: Explicit diagnosis of the local ozone production rate and the ozone-$NO_x$-VOC sensitivities, Sci. Bull., 63, 1067–1076, https://doi.org/10.1016/j.scib.2018.07.001, 2018.

Wang, F., Hu, R., Xie, P., Wang, Y., Chen, H., Zhang, G., and Liu, W.: Calibration source for OH radical based on synchronous photolysis, Acta Phys. Sin.-Ch. Ed., 69, 090701, https://doi.org/10.7498/aps.69.20200153, 2020.

Wang, F. Y., Hu, R. Z., Chen, H., Xie, P. H., Wang, Y. H., Li, Z. Y., Jin, H. W., Liu, J. G., and Liu, W. Q.: Development of a field system for measurement of tropospheric OH radical using laser-induced fluorescence technique, Opt. Express, 27, A419–A435, https://doi.org/10.1364/oe.27.00a419, 2019a.

Wang, H., Lu, K., Tan, Z., Chen, X., Liu, Y., and Zhang, Y.: Formation mechanism and control strategy for particulate nitrate in China, J. Environ. Sci., 123, 476–486, https://doi.org/10.1016/j.jes.2022.09.019, 2022a.

Wang, H., Ma, X., Tan, Z., Wang, H., Chen, X., Chen, S., Gao, Y., Liu, Y., Liu, Y., Yang, X., Yuan, B., Zeng, L., Huang, C., Lu, K., and Zhang, Y.: Anthropogenic monoter-

penes aggravating ozone pollution, Nat. Sci. Rev., 9, nwac103, https://doi.org/10.1093/nsr/nwac103, 2022b.

Wang, S.-n., Wu, R.-r., and Wang, L.-m.: Role of Hydrogen Migrations in Carbonyl Peroxy Radicals in the Atmosphere, Chinese J. Chem. Phys., 32, 457–466, https://doi.org/10.1063/1674-0068/cjcp1811265, 2019b.

Wang, T., Xue, L., Feng, Z., Dai, J., Zhang, Y., and Tan, Y.: Ground-level ozone pollution in China: a synthesis of recent findings on influencing factors and impacts, Environ. Res. Lett., 17, 063003, https://doi.org/10.1088/1748-9326/ac69fe, 2022c.

Wang, W., Yuan, B., Peng, Y., Su, H., Cheng, Y., Yang, S., Wu, C., Qi, J., Bao, F., Huangfu, Y., Wang, C., Ye, C., Wang, Z., Wang, B., Wang, X., Song, W., Hu, W., Cheng, P., Zhu, M., Zheng, J., and Shao, M.: Direct observations indicate photodegradable oxygenated volatile organic compounds (OVOCs) as larger contributors to radicals and ozone production in the atmosphere, Atmos. Chem. Phys., 22, 4117–4128, https://doi.org/10.5194/acp-22-4117-2022, 2022d.

Wang, W., Yuan, B., Su, H., Cheng, Y., Qi, J., Wang, S., Song, W., Wang, X., Xue, C., Ma, C., Bao, F., Wang, H., Lou, S., and Shao, M.: A large role of missing volatile organic compound reactivity from anthropogenic emissions in ozone pollution regulation, Atmos. Chem. Phys., 24, 4017–4027, https://doi.org/10.5194/acp-24-4017-2024, 2024.

Wang, Y., Hu, R., Xie, P., Chen, H., Wang, F., Liu, X., Liu, J., and Liu, W.: Measurement of tropospheric $HO_2$ radical using fluorescence assay by gas expansion with low interferences, J. Environ. Sci. (China), 99, 40–50, https://doi.org/10.1016/j.jes.2020.06.010, 2021.

Whalley, L. K., Blitz, M. A., Desservettaz, M., Seakins, P. W., and Heard, D. E.: Reporting the sensitivity of laser-induced fluorescence instruments used for $HO_2$ detection to an interference from $RO_2$ radicals and introducing a novel approach that enables $HO_2$ and certain $RO_2$ types to be selectively measured, Atmos. Meas. Tech., 6, 3425–3440, https://doi.org/10.5194/amt-6-3425-2013, 2013.

Whalley, L. K., Stone, D., Dunmore, R., Hamilton, J., Hopkins, J. R., Lee, J. D., Lewis, A. C., Williams, P., Kleffmann, J., Laufs, S., Woodward-Massey, R., and Heard, D. E.: Understanding in situ ozone production in the summertime through radical observations and modelling studies during the Clean air for London project (ClearfLo), Atmos. Chem. Phys., 18, 2547–2571, https://doi.org/10.5194/acp-18-2547-2018, 2018.

Whalley, L. K., Slater, E. J., Woodward-Massey, R., Ye, C., Lee, J. D., Squires, F., Hopkins, J. R., Dunmore, R. E., Shaw, M., Hamilton, J. F., Lewis, A. C., Mehra, A., Worrall, S. D., Bacak, A., Bannan, T. J., Coe, H., Percival, C. J., Ouyang, B., Jones, R. L., Crilley, L. R., Kramer, L. J., Bloss, W. J., Vu, T., Kotthaus, S., Grimmond, S., Sun, Y., Xu, W., Yue, S., Ren, L., Acton, W. J. F., Hewitt, C. N., Wang, X., Fu, P., and Heard, D. E.: Evaluating the sensitivity of radical chemistry and ozone formation to ambient VOCs and $NO_x$ in Beijing, Atmos. Chem. Phys., 21, 2125–2147, https://doi.org/10.5194/acp-21-2125-2021, 2021.

Woodward-Massey, R., Sommariva, R., Whalley, L. K., Cryer, D. R., Ingham, T., Bloss, W. J., Ball, S. M., Cox, S., Lee, J. D., Reed, C. P., Crilley, L. R., Kramer, L. J., Bandy, B. J., Forster, G. L., Reeves, C. E., Monks, P. S., and Heard, D. E.: Radical chemistry and ozone production at a UK coastal receptor site, Atmos. Chem. Phys., 23, 14393–14424, https://doi.org/10.5194/acp-23-14393-2023, 2023.

Yang, X., Lu, K., Ma, X., Liu, Y., Wang, H., Hu, R., Li, X., Lou, S., Chen, S., Dong, H., Wang, F., Wang, Y., Zhang, G., Li, S., Yang, S., Yang, Y., Kuang, C., Tan, Z., Chen, X., Qiu, P., Zeng, L., Xie, P., and Zhang, Y.: Observations and modeling of OH and $HO_2$ radicals in Chengdu, China in summer 2019, Sci. Total Environ., 772, 144829–144829, https://doi.org/10.1016/j.scitotenv.2020.144829, 2021a.

Yang, Y., Li, X., Zu, K., Lian, C., Chen, S., Dong, H., Feng, M., Liu, H., Liu, J., Lu, K., Lu, S., Ma, X., Song, D., Wang, W., Yang, S., Yang, X., Yu, X., Zhu, Y., Zeng, L., Tan, Q., and Zhang, Y.: Elucidating the effect of HONO on $O_3$ pollution by a case study in southwest China, Sci. Total Environ., 756, 144127, https://doi.org/10.1016/j.scitotenv.2020.144127, 2021b.

Yang, X., Lu, K., Ma, X., Gao, Y., Tan, Z., Wang, H., Chen, X., Li, X., Huang, X., He, L., Tang, M., Zhu, B., Chen, S., Dong, H., Zeng, L., and Zhang, Y.: Radical chemistry in the Pearl River Delta: observations and modeling of OH and $HO_2$ radicals in Shenzhen in 2018, Atmos. Chem. Phys., 22, 12525–12542, https://doi.org/10.5194/acp-22-12525-2022, 2022.

Yang, X., Li, Y., Ma, X., Tan, Z., Lu, K., and Zhang, Y.: Unclassical Radical Generation Mechanisms in the Troposphere: A Review, Environ. Sci. Technol., 58, 15888–15909, https://doi.org/10.1021/acs.est.4c00742, 2024a.

Yang, X., Wang, H., Lu, K., Ma, X., Tan, Z., Long, B., Chen, X., Li, C., Zhai, T., Li, Y., Qu, K., Xia, Y., Zhang, Y., Li, X., Chen, S., Dong, H., Zeng, L., and Zhang, Y.: Reactive aldehyde chemistry explains the missing source of hydroxyl radicals, Nat. Commun., 15, 1648, https://doi.org/10.1038/s41467-024-45885-w, 2024b.

Zhang, G., Hu, R., Xie, P., Lou, S., Wang, F., Wang, Y., Qin, M., Li, X., Liu, X., Wang, Y., and Liu, W.: Observation and simulation of $HO_x$ radicals in an urban area in Shanghai, China, Sci. Total Environ., 810, 152275, https://doi.org/10.1016/j.scitotenv.2021.152275, 2022a.

Zhang, G., Hu, R., Xie, P., Lu, K., Lou, S., Liu, X., Li, X., Wang, F., Wang, Y., Yang, X., Cai, H., Wang, Y., and Liu, W.: Intercomparison of OH radical measurement in a complex atmosphere in Chengdu, China, Sci. Total Environ., 838, 155924, https://doi.org/10.1016/j.scitotenv.2022.155924, 2022b.